EMG model calibration and trajectory tracking of rehabilitation exoskeleton by asynchronous tele-training

Ubaldo Castro Jiménez & Edgar A. Martínez-García

Published online: 18 Sep 2024.

Submit your article to this journal ⬚

View related articles ⬚

View Crossmark data ⬚

Taylor & Francis
Taylor & Francis Group

🔓 OPEN ACCESS | Check for updates

EMG model calibration and trajectory tracking of rehabilitation exoskeleton by asynchronous tele-training

Ubaldo Castro Jiménez and Edgar A. Martínez-García ⓘ

Laboratorio de Robótica, Instuto de Ingeniería y Tecnología, Universidad Autónoma de Ciudad Juárez, Juárez, Mexico

ABSTRACT

This study presents a novel kinematic tracking model, designed for a networked exoskeleton system that is asynchronously taught by a remote therapist. The therapist's rehabilitation exercises are quantitatively assessed using a monocular vision system. The resultant metrics are then transmitted asynchronously over the network to patients equipped with exoskeletons. The exoskeleton utilises these metrics as reference paths for exercises, complemented by electromyography (EMG) feedback. This work introduces a calibration approach aimed at estimating angular positions by utilising EMG observations. The calibration model establishes real-time correlations between polynomial reference positions. We further explore redundant kinematics, incorporating an EMG observer for linear, time-variant rehabilitation tracking control. Our methodology is validated using vision-based metric data and experimental EMG measurements including shoulder flexion, elbow flexion, and rowing-like movements. Computer simulations demonstrate the system's ability to reliably, robustly, and effectively follow desired trajectories. This research offers a promising approach for remote personalized rehabilitation.

1. Introduction

From time to time, mankind has had to confront global infectious diseases with deadly impact, as has recently been the case with the Coronavirus, COVID-19. Family members have been compelled to take on in-home responsibilities due to quarantine, including patients following medical treatments. Pandemic-related robotic systematised solutions have been described for multiple scenarios (Magid et al. 2021). Similarly, telesystems, communication networks, intelligent machines, and information technologies provide support for easy post-pandemic scenarios (Haider et al. 2020; Yang et al. 2020) by keeping us away from contagious scenarios (Touil et al. 2020; Wu et al. 2020).

The current technological market has provided a spectrum of modern communication technology such as distributed networked equipment, Internet-based telesystems, telepresence devices, either synchronous or asynchronous modalities (Barr et al. 2020). Telesystems applications have evolved into Internet shopping, remote academic/job meetings, virtual scholarly classes, and healthcare support, such as tele-rehabilitation therapies.

An exoskeleton is a wearable robot fitted on a human's body, designed to enhance biomechanical functions, with the human serving as the controller (Yang et al. 2008; Pons 2008). To be effective, an exoskeleton must provide a sense of lightness and agility, akin to the human bone structure. The advantages of exoskeleton technology extend to enhancing biom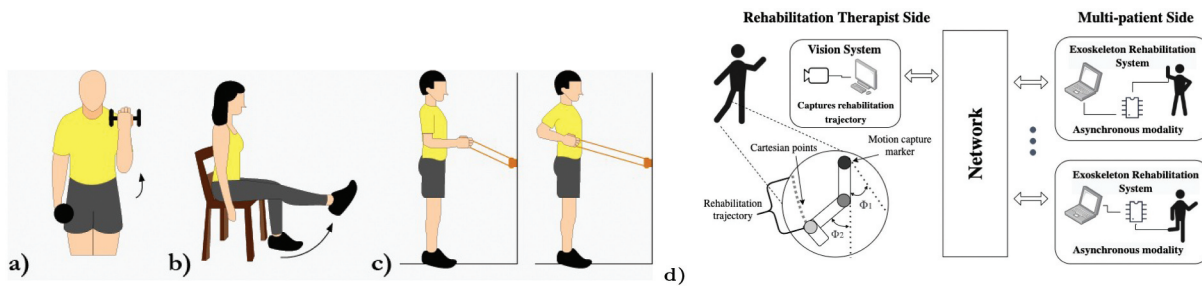echanical capabilities, addressing diverse needs such as the substitution of body parts' mobility, providing locomotion assistance (Samadi et al. 2015; Li et al. 2019), and aiding in rehabilitation (Díez et al. 2016; Buongiorno et al. 2018; Pu et al. 2020; Charafeddine 2019). Rehabilitation is particularly crucial in cases of post-corrective surgeries, where constant therapy is required to expedite recovery. Demand for exoskeletons spans various sectors, including athletics, sports, manual labour, and the military, where common surgeries involve conditions like rotator cuff injuries, acromioclavicular articulation injuries, elbow dislocations, hip dislocations, reconstruction of injured anterior cruciate ligaments, knee arthroscopy, and total knee replacement. Prolonged post-surgery rehabilitation plays a critical role in recovery, as prolonged limb immobilisation can lead to a significant reduction in muscle strength and mobility. Additionally, various studies have explored control algorithms for lower-limb wearable robot systems (Jiménez and Verlinden 2011), as well as for upper limbs (Bauer and Pan 2020), to provide power assistance (Li et al. 2014). Wearable robotic hands have been developed for purposes such as haptic feedback, assistive functions, and rehabilitation (Sarac et al. 2019). These devices also find applications in tasks like grasping (Gandolla et al. 2016), the development of multimodal rehabilitation exoskeletons (Li et al. 2017; Sun et al. 2020), and walking assistance (Aguirre-Ollinger et al. 2011).

The work by (He et al. 2015) introduced an adaptive neural control system for rehabilitating lower limbs with unknown model dynamics, focusing on adapting to the complex dynamics of human-exoskeleton interactions. In this study, we

Figure 1. Tele-training rehabilitation exercises. a)-b) elbow, knee flexion-extension. c) shoulder sagittal rotation. d) telesystem architecture.

propose a feedback kinematic tracking model for a networked exoskeleton, which is taught asynchronously by a remote therapist (Figure 1a-c). The therapist's rehabilitation exercises are visually assessed and transformed into analytical polynomial Cartesian functions through a least-square fitting approach. A noteworthy innovation presented in this work is the transmission of a concise stream of polynomial coefficients, as opposed to the entire set of Cartesian data. On the patient's side, these Cartesian polynomials are employed to recreate the therapist's experimental data with higher resolution. Additionally, by introducing a constant time period, denoted as T, we achieve the reconstruction of Cartesian components, x and y, as periodic functions of time using Fourier series. The integration of Cartesian and electromyography (EMG) data as feedback, similar to the approach in Kang et al. (2019), represents another significant contribution of this work. Notably, our model is designed to infer the posture of Cartesian limbs from EMG signals, allowing for recalibration during new exercises. This feature offers a generalised approach, enabling the control law to adapt to the structure of different exoskeletons simply by readjusting their Jacobian matrices. Furthermore, a linear trajectory smoother model is introduced in cases where patients have biomechanical movement constraints. These smoothing functions facilitate a gradual convergence towards the desired reference trajectory shape. To evaluate the efficacy of the proposed exoskeleton, we conducted extensive simulations involving hundreds of tracking control rehabilitation exercises.

This study introduces a distinctive approach to remote therapy within the realm of tele-rehabilitation. Specifically, it proposes a feedback kinematic tracking model for a networked exoskeleton that undergoes asynchronous visual instruction from a remote therapist. The emphasis lies in transmitting concise streams of polynomial coefficients instead of the entire set of Cartesian data, subsequently transformed into analytical polynomial Cartesian functions. Additionally, the study underscores the integration of Cartesian and electromyography (EMG) data as feedback, facilitating the inference of limb posture from EMG signals and recalibration during new exercises. In the existing literature various approaches within closely related fields of study, including works by (Bouteraa and Abdallah 2016; Zhang et al. 2019; Akbari et al. 2021; Liu et al. 2022; Kim et al. 2022; Cisnal et al. 2023), partially intersect with the themes presented in this work. However, the authors remain uncertain as to whether fully analogous studies have been previously published.

The proposed solution specifically focuses on tele-rehabilitation, where a therapist's exercises are visually assessed and transmitted to the patient's exoskeleton. The key innovation of the proposed solution lies in the transmission of concise streams of polynomial coefficients, rather than transmitting the entire set of Cartesian data. This approach provides flexibility in tracking and control, making the rehabilitation process highly accurate and efficient. Overall, the proposed solution offers a generalised approach to tele-rehabilitation, making it more accessible and accommodating to a wide range of patient needs. It combines clinical precision with technological sophistication, providing an effective and efficient means of rehabilitation. The proposed feedback kinematic tracking model for a networked exoskeleton taught asynchronously by a remote therapist is required to ensure accurate, personalised, and efficient rehabilitation for patients, regardless of their location or access to specialised facilities. In addition, it provides: Accuracy and Precision: A feedback kinematic tracking model allows for precise tracking of the patient's movements during rehabilitation exercises. It ensures that the exoskeleton accurately follows the desired trajectory and provides the necessary assistance or resistance. This level of accuracy is crucial for effective rehabilitation. Adaptability and Customization: The feedback model allows for real-time adjustments and adaptations based on the patient's specific needs and progress. The integration of electromyography (EMG) data as feedback allows for the inference of Cartesian posture from EMG signals, enabling recalibration during new exercises and adapting to different exoskeleton structures. Remote Guidance and Supervision: Asynchronous teaching by a remote therapist enables patients to receive guidance and supervision from experts regardless of their location. This is particularly beneficial for patients who may not have access to specialised rehabilitation facilities or therapists in their vicinity. Flexibility and Convenience: Asynchronous teaching allows patients to perform rehabilitation exercises at their own convenience, without the need for simultaneous network connections. They can follow the prescribed exercises and receive feedback from the therapist at a time that suits them best. Efficiency and Cost-effectiveness: By utilising a networked exoskeleton and asynchronous teaching, the rehabilitation process becomes more efficient and cost-effective. Patients can save time and resources by avoiding frequent visits to rehabilitation centres, while still receiving expert guidance and support.

This paper is structured as follows: Section 2 delves into the therapist-side tele-rehabilitation, elucidating the teaching

process facilitated by a vision system. In Section 3, we unveil the proposed EMG calibration and observation measurement models. Following this, Section 4 delves into the exoskeleton's motion constraints and its kinematic control law. A comprehensive summary of the research's results is provided in Section. Finally, Section 6 offers a set of conclusions drawn from this study.

2. Human therapist remote visual teaching

The proposed networked distributed system is structured as an asynchronous tele-system architecture, with the therapist's side and the patients constituting the client side. The server plays a pivotal role by providing geometric data acquired visually from the therapist's exercise sessions in front of a camera, transmitted over the network. An artificial vision system captures the data related to the training trajectories taught by the therapist (Figure 1d, left side).

Notably, the interaction session between the therapist and the patient occurs asynchronously, eliminating the need for simultaneous network connections. This approach stands in contrast to traditional tele-operation methods (Lanini et al. 2015). The exoskeleton has the flexibility to connect at any given date and time, allowing the download of therapy exercises in the form of analytic trajectories, represented by coefficients (Figure 1d, right side). The server's computer is equipped with a monocular vision system that accurately measures the angles and positions of coloured landmarks strategically placed at the therapist's limb joints (Figure 3a,b-left). Remarkably, the therapist does not require any specialised equipment during the exercise sessions.

In light of the evident benefits of rehabilitation exoskeletons (Fisahn et al. 2016), we selected commonly practiced exercises from a recognised exercise program (Athwal 2017) to serve as the basis for our study. These exercises, whether post-injury or post-surgery, were adopted as trajectories (Figure 1a-c). For example, exercises such as the rotator cuff, shoulder and elbow flexion exercises were employed to teach various motions (Figure 1a,c). Similarly, we incorporated exercises like knee extensions (Figure 1b) and the stand-up paddle exercise with an elastic band (Figure 1c) to broaden the scope of our research.

The proposed tele-system was crafted on standard-capability computers running the Linux Gentoo operating system, version 4.4. The entire codebase was developed using the GNU C/C++ compiler, making extensive use of multiple open-source libraries, including openCV, Armadillo C++, the Open Dynamics Engine (ODE), and Gazebo. Communication between components was facilitated using the TCP/IP protocol via sockets. The vision sensor employed was a cost-effective USB camera (see Table 1). For the acquisition of EMG biosignals, we utilised the gMOBIlab+ device with two EMG channels. To bring our vision to life, we implemented a virtual exoskeleton prototype with original design mechanisms. This virtual exoskeleton operates under the control of human EMG signals, functioning as a master-slave system.

This work places some emphasis on vision-based teaching. To streamline the measurement process, we strategically position coloured landmarks at the joints of the therapist's limbs, as depicted in Figure 3. These landmarks serve as the key reference points for measuring angles and positions during exercise sessions. Our approach to measuring the metric trajectories of exercises involves a two-step process. First, we segment the joints' landmarks based on their RGB colour. Subsequently, we employ a nominal resolution geometric model to track the centroid positions of these metric landmarks. In this approach, we establish the reference coordinate system at the location of the visual sensor. In line with the extrinsic parameters outlined in Figure 2, we define an RGB image as a cubic matrix $\mathbf{I} \in \mathbb{R}^{\triangleright \times \ltimes \times \models}$, comprising the union of the three primary color channels: red $\mathbf{I}_R$, green $\mathbf{I}_G$, and blue $\mathbf{I}_B$. To extract the shoulder's landmark, we apply a threshold ζ_S to the red channel $\mathbf{I}_R$ and incorporate a zeros matrix $\mathbf{0} \in \mathbb{R}^{\triangleright \times \ltimes}$. This process yields a binary segmented image denoted as $\mathbf{I}_S$ and is achieved through the following Boolean equation:

$$\mathbf{I}_S = (\mathbf{I}_R > \zeta_S) \cup (\mathbf{I}_G \cap \mathbf{0}) \cup (\mathbf{I}_B \cap \mathbf{0}). \tag{1}$$

Table 1. Experimental visual sensor's intrinsic/extrinsic parameters[a].

Resolution	640×480	height	1.1024982 m
Focal lenght	1.5 m	width	1.4849993 m
Frames/s	30	z (distance)	2.0 m
$\varphi_{horizontal}$	52.6708^o	$\varphi_{vertical}$	40.3567^o
H. resol f_h	1.10249 m	V. resol. f_v	1.48499 m

[a]Logitech USB 2.0 camera, views of Figure 3.
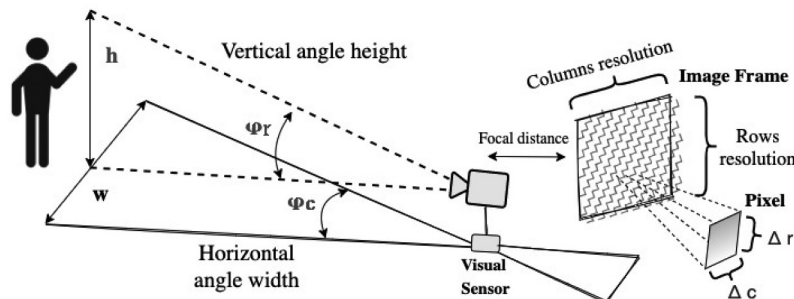
Figure 2. Monocular vision-based geometrical model on the therapist's side.
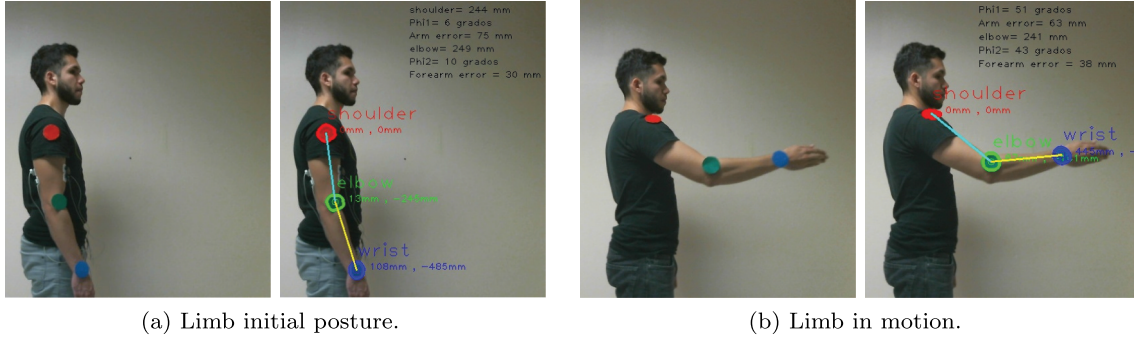
(a) Limb initial posture.   (b) Limb in motion.

Figure 3. Visual instruction of various exercises by the therapist.

Similarly, the isolation of the elbow's joint landmark is achieved through the utilisation of a binary image denoted as $\mathbf{I}_E$. The effectiveness of this process hinges on the presence of a critical threshold denoted as ζ_E, which assumes a pivotal role in the Boolean criterion:

$$\mathbf{I}_E = (\mathbf{I}_R \cap \mathbf{0}) \cup (\mathbf{I}_G < \zeta_E) \cup (\mathbf{I}_B \cap \mathbf{0}). \tag{2}$$

In a similar manner, the identification of the wrist landmark is carried out through the utilisation of a binary image represented as $\mathbf{I}_W$ The determination of this landmark relies on the precise specification of a threshold value denoted as ζ_W which is an integral part of the following criterion:

$$\mathbf{I}_W = ((\mathbf{I}_R \cap \mathbf{0}) \cup (\mathbf{I}_G \cap \mathbf{0})) \cup (\mathbf{I}_B > \zeta_W). \tag{3}$$

For each segmented region in the images $\mathbf{I}_R$, $\mathbf{I}_G$, and $\mathbf{I}_B$, the position of the landmarks in spatial coordinates is determined by their centroids, denoted as column p_c and row p_r, as expressed by:

$$p_c = \frac{1}{2}\sum_i c_i, \quad p_r = \frac{1}{2}\sum_i r_i, \tag{4}$$

In this context, the spatial coordinates c_i and r_i, where both c_i and r_i belong to a segmented region R, represent the pixels within the region. We will now proceed to offer a comprehensive description of the geometric visual model, as depicted in Figure 2.

Geometrically, the equality for the vertical field of view ((5)) is valid.

$$\tan\left(\frac{\varphi_r}{2}\right) = \left(\frac{h/2}{z}\right), \tag{5}$$

Here, h represents the height of the object of interest, and z denotes the metric depth of the human therapist from the camera. Thus, building upon the previous expression, we can determine φ_r, which represents the vertical camera angle quantised in terms of image rows.

$$\varphi_r = 2\tan^{-1}\left(\frac{h}{2z}\right). \tag{6}$$

With respect to (w.r.t.) the horizontal field of view,

$$\tan\left(\frac{\varphi_c}{2}\right) = \left(\frac{w/2}{z}\right), \tag{7}$$

then, dropping off the angle along image's columns φ_c

$$\varphi_c = 2\tan^{-1}\left(\frac{w}{2z}\right). \tag{8}$$

We estimate the vertical metric resolution factor, denoted as f_h, as well as the horizontal metric resolution factor, denoted as f_w,[1]

$$f_h = 2\tan\left(\frac{\varphi_r}{2}\cdot z\right), \quad f_w = 2\tan\left(\frac{\varphi_c}{2}\cdot z\right). \tag{9}$$

Subsequently, we determine the vertical metric position Δ_r and the horizontal metric position Δ_c of the centre pixel (p_r, p_c) of a landmark.

$$\Delta_r = \frac{f_h}{\mathsf{p}_r}, \quad \Delta_c = \frac{f_w}{\mathsf{p}_c}. \tag{10}$$

Next, in the therapist's side, the superior limb kinematic motion model in 3D space is provided by the expression

$$\begin{pmatrix} x \\ y \\ z \end{pmatrix} = \begin{pmatrix} \ell_1\sin(\phi_0)\cos(\phi_1) + \ell_2\sin(\phi_0)\cos(\phi_1 + \phi2) \\ \ell_1\sin(\phi_1) + \ell_2\sin(\phi_1 + \phi2) \\ \ell_1\cos(\phi_0)\cos(\phi_1) + \ell_2\cos(\phi_0)\cos(\phi_1 + \phi2) \end{pmatrix},$$

where depth is affected by the yaw angle ϕ_0 and double pitch joits ϕ_1, ϕ_2, and ℓ_1 and ℓ_2 to denote the actual metric lengths of the upper arm and forearm, respectively. When representing a 2D exercise scenario, the yaw angle $\phi_0 = \pi/2$. Therefore, the depth dimension becomes irrelevant since the arm's length is not projected, and the trajectory is drawn on a plane in front of the camera. The links ℓ_1, ℓ_2 visual measurements,

$$\ell_1 = \sqrt[2]{(x_S - x_E)^2 + (y_S - y_E)^2} \tag{11}$$

and

$$\ell_2 = \sqrt[2]{(x_E - x_W)^2 + (y_E - y_W)^2}. \tag{12}$$

Similarly, we use the variables θ_1 and θ_2 to denote the joint angles of the limb.

$$\theta_1 = \tan^{-1}\left(\frac{y_E - y_S}{x_E - x_S}\right), \quad \theta_2 = \tan^{-1}\left(\frac{y_W - y_E}{x_W - x_E}\right) \tag{13}$$

We illustrate a shoulder exercise in Figure 3, and in Figure 9, we display the resulting Cartesian trajectory, with red points indicating the Cartesian positions of the blue wrist landmark.

In summary, the rehabilitation trajectory, denoted as $\mathcal{S} = \Theta_0, \Theta_1, \Theta_2, \ldots, \Theta_N$, is comprised of a set of joint angles $\Theta_i = (\theta_1, \theta_2)^\mathsf{T}$ and limb parameters ℓ_1 and ℓ_2.

In Figure 4, a series of repetitions stemming from exercises performed by the therapist is presented. These exercises encompass a single experimental repetition involving shoulder flexion (depicted in Figure 4a), along with three experimental repetitions focusing on elbow flexion (illustrated in Figure 4b). Additionally, three experimental repetitions of a rowing-like motion are depicted (Figure 4c), wherein both the shoulder and elbow joints operate in unison during the exercise. It is imperative to emphasise that the reference coordinates, denoted as $(0, 0)$, are firmly anchored at the centroid of the shoulder.

Additionally, in Figure 5, we present angular motion measurements for all joints utilising visual odometry, with a focus on the $x - y$ plane. These angular measurements correspond to the Cartesian motion data depicted in Figure 4. In Figure 5a (left), we observe an experiment exclusively involving shoulder flexion, where a linear rigid arm is used, and there are a total of five repetitions. It's important to note that this exercise is the simplest, resulting in data points with a higher degree of overlap. On the right side of Figure 5a, while still involving shoulder flexion, we observe slight angular perturbations in the wrist, averaging approximately $9°$. These perturbations were primarily caused by minor limb vibrations from the therapist and were further exacerbated by contrast and brightness noise in the measurements. Figure 5b displays angular measurements for elbow flexion exercises. To ensure clarity without excessive data overlap, we have chosen to present three distinct experiments, each with multiple repetitions. On the left side of Figure 5b, we observe angular perturbations in the wrist during elbow flexion exercises. Conversely, the right side of Figure 5b depicts three separate experiments involving elbow-flexion exercises, displaying multiple repetitions that result in periodic oscillations. This presentation highlights variations in speed during

the experiments, reflecting biomechanical consistency and differences in execution.

Figure 5c, in its entirety, represents three distinct experiments of rowing-like motions, each of which consists of six repetitions. This comprehensive view enables us to examine the angular dynamics in these exercises in greater detail. On the left side of Figure 5c, we can observe the angular magnitudes of elbow flexions. Meanwhile, the right side of the same figure portrays shoulder flexions, which synchronise their motion with the elbow flexions. On the therapist's side, the process involves employing a least square polynomial fitting approach to derive a Cartesian function $y(x)$. This method is used to process the vision-based 3D measured data, resulting in the determination of polynomial coefficients of the n-th degree, as described in the following equation:

$$
\begin{pmatrix} a_0 \\ a_1 \\ \vdots \\ a_n \end{pmatrix} = \begin{pmatrix} n & \sum_i x_i & \cdots & \sum_i x_i^n \\ \sum_i x_i & \sum_i x_i^2 & \cdots & \sum_i x_i^{n+1} \\ \vdots & & & \\ \sum_i x_i^j & \sum_i x_i^{j+1} & \cdots & \sum_i x_i^{2n} \end{pmatrix}^{-1} \cdot \begin{pmatrix} \sum_i y_i \\ \sum x_i y_i \\ \vdots \\ \sum_i x_i^n y_i \end{pmatrix},
$$
(14)

In this manner, we obtain a parametric function that accurately fits the exercise's Cartesian data, following a polynomial form:

$$
y(x) = a_0 + a_1 x + a_2 x^2 + a_3 x^3 + \ldots + a_n x^n.
$$
(15)

This approach significantly reduces the trade-off during data streaming to only a few coefficients and the time period T of one exercise oscillation. These coefficients require a minimal amount of bytes for transmission over the network, thereby mitigating significant time delays. Figure 6 illustrates experimental data from teaching trajectories that have been
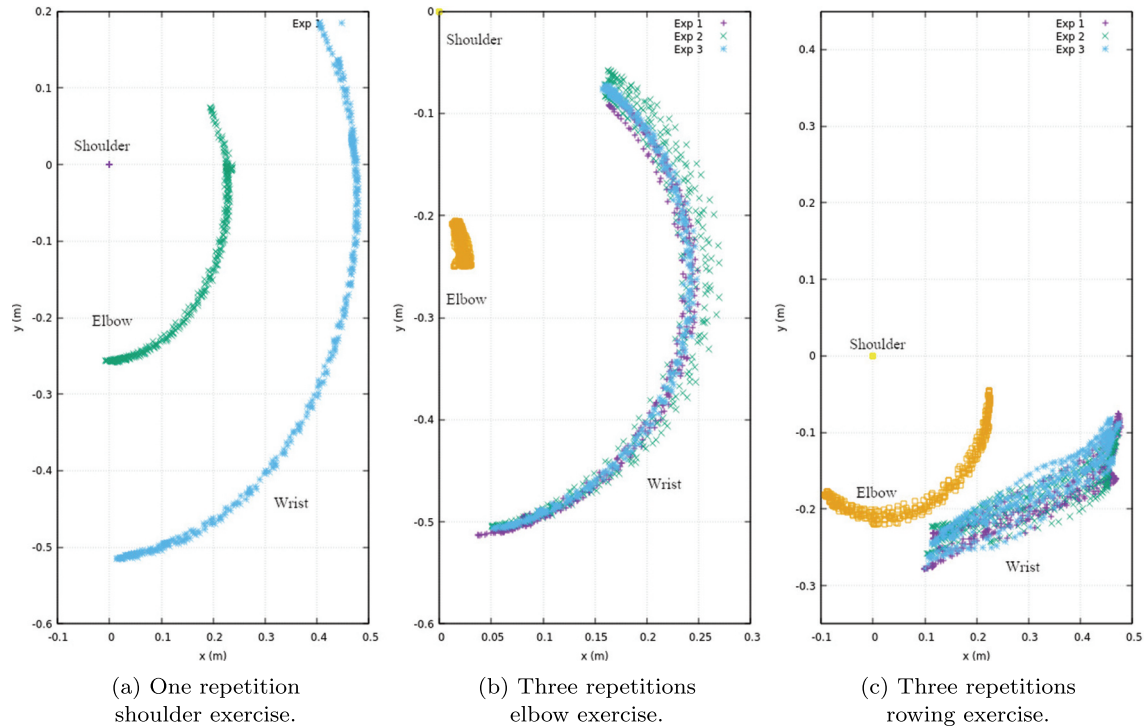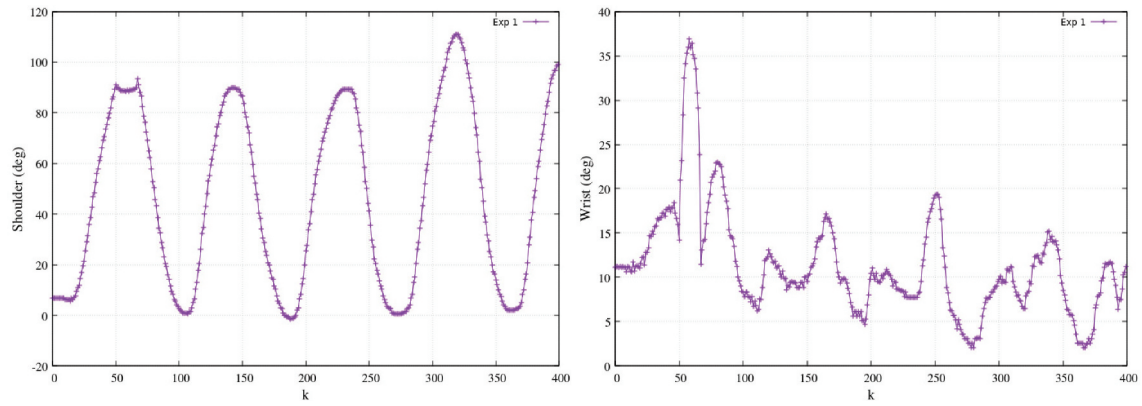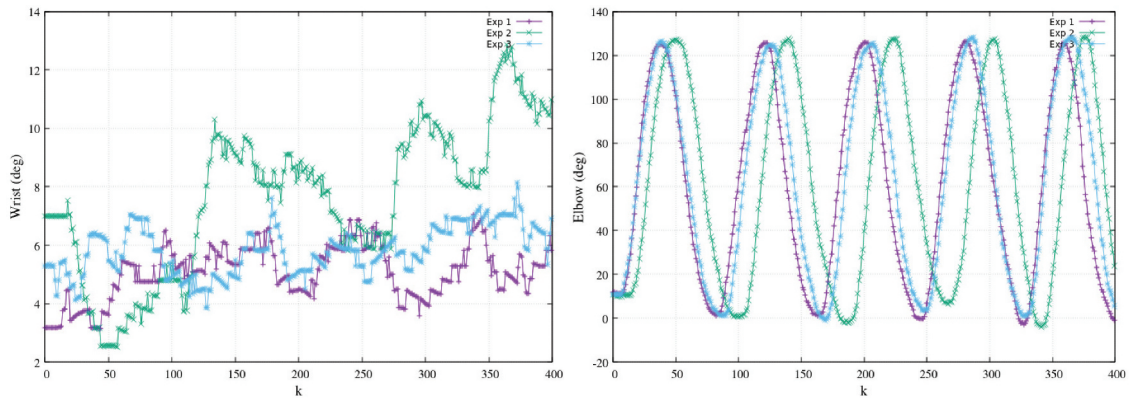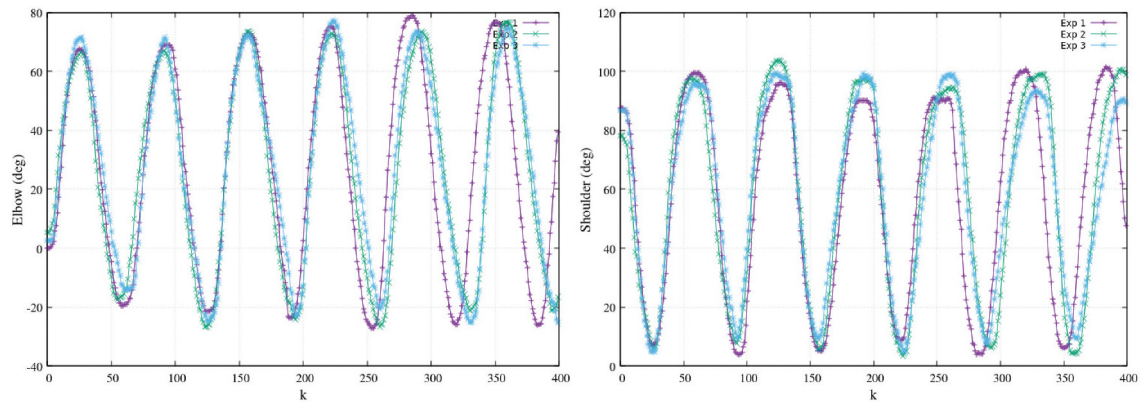

(a) One repetition shoulder exercise.

(b) Three repetitions elbow exercise.

(c) Three repetitions rowing exercise.

Figure 4. Experimental measurements in flexion-extension exercises of shoulder, elbow and wrist.

(a) Shoulder exercise.

(b) Elbow exercise.

(c) Rowing exercise.

Figure 5. Angular measurements for flexion-extension exercises of shoulder, elbow and wrist.

effectively fitted by various polynomials, exemplifying the practicality and efficiency of this approach.

By representing the exercise trajectory as a continuous polynomial function, denoted as $y(x)$, available on the exoskeleton's side, we open the door to the replication of experimental data at higher metrical resolutions. With the time constant of a period T at our disposal, the exoskeleton's side can autonomously convert the high-resolution Cartesian data into new components as functions of time. Using Fourier series, we generate new Cartesian components, $x(t)$ and $y(t)$, as functions of time. Figure 7 effectively demonstrates this process, showcasing a Cartesian reference trajectory as $x(t)$ versus $y(t)$, realistically reproducing three experiments involving elbow flexion. This approach, as presented in this work, offers sophisticated analytical functions that serve as effective substitutes for the therapist's exercises, which typically involve large amounts of experimental data. In doing so, it efficiently addresses the challenges of long transmission time delays and the handling of extensive data tables, ultimately yielding parametric functions that streamline the entire process.
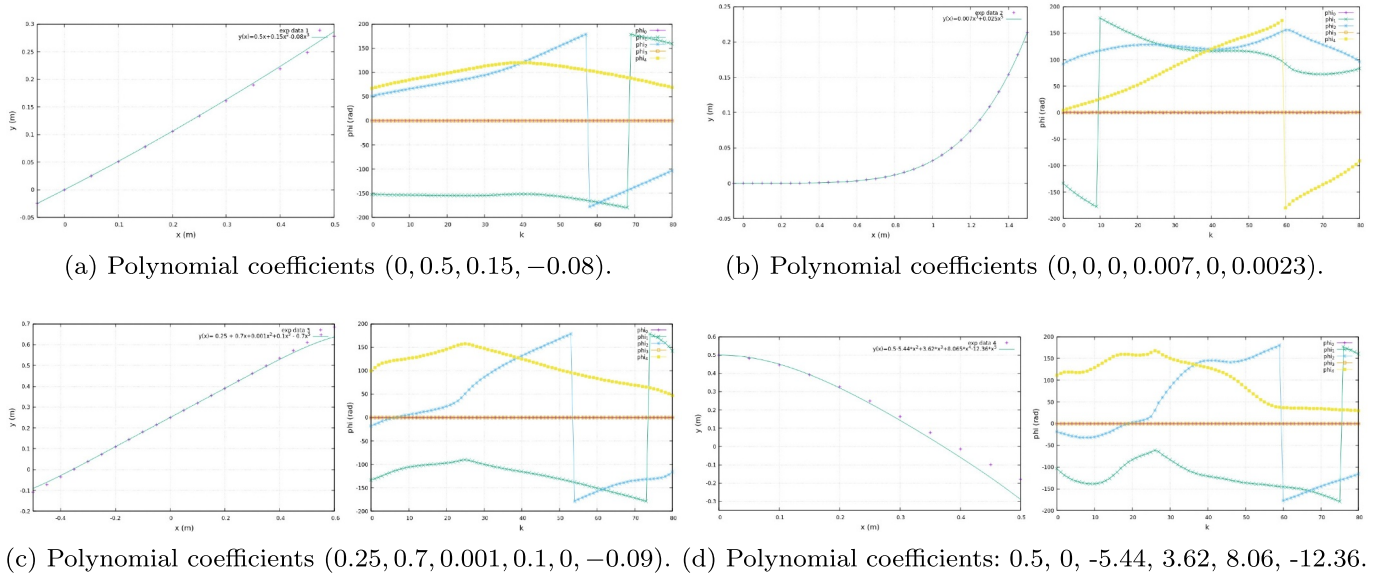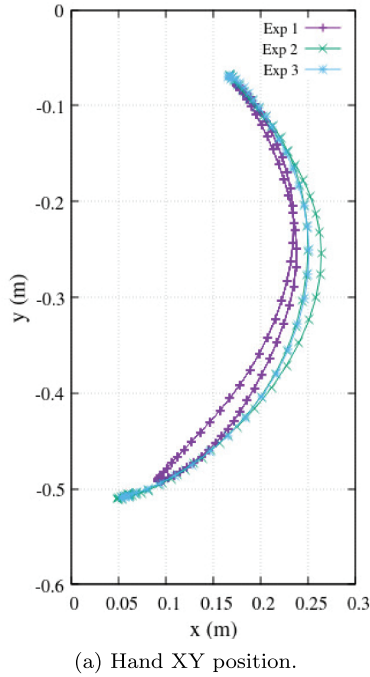
(a) Polynomial coefficients $(0, 0.5, 0.15, -0.08)$.

(b) Polynomial coefficients $(0, 0, 0, 0.007, 0, 0.0023)$.

(c) Polynomial coefficients $(0.25, 0.7, 0.001, 0.1, 0, -0.09)$. (d) Polynomial coefficients: 0.5, 0, -5.44, 3.62, 8.06, -12.36.

Figure 6. $y(x)$ models fitting experimental trajectories. Depiction of xy positions and produced joints' angle.

(a) Hand XY position.

Figure 7. Analytical $x(t)$ vs $y(t)$ functions fitting elbow-flexion experimental data of Figure 4.

Moreover, in scenarios where biomechanical constraints affecting a patient's movements are detected during exoskeleton deployment, we employ smoothing functions to facilitate gradual transitions that accommodate these constraints. One such smoothing function, based on a linear approach, is detailed below:

$$y_{ref} = \kappa_\tau + \kappa_s y(x), \qquad (16)$$

In this function, the original therapist's trajectory is regarded as the ideal Cartesian reference motion, denoted as $y(x)$. Therefore, we introduce two key parameters: κ_τ, representing the translation factor of a family of functions, and κ_s,
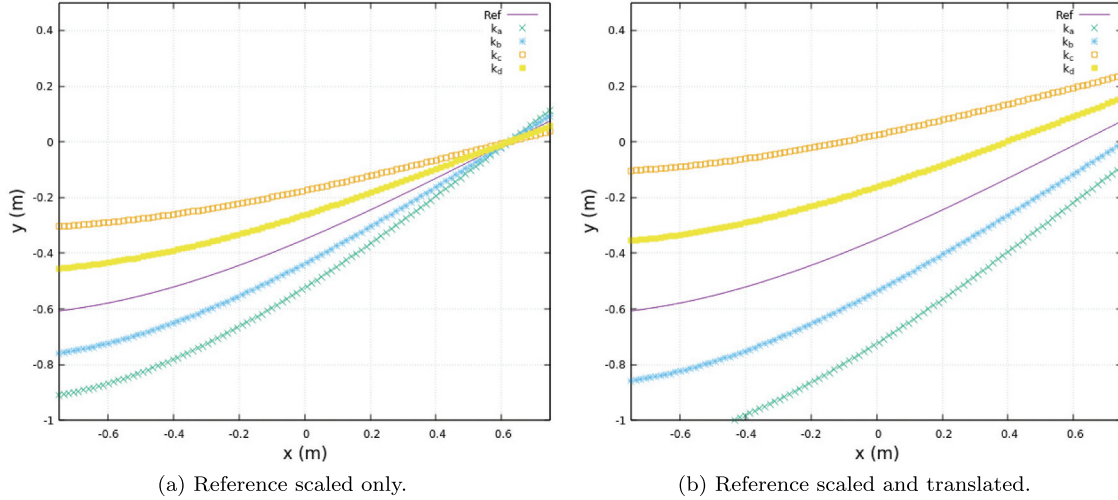
representing the scaling function's coefficient. When $\kappa_\tau = 0$ and $\kappa_s = 1$, the exercise function aligns precisely with the therapist's reference trajectory. However, by adjusting the values of these smoothing coefficients, we achieve gradual convergence towards the therapist's ideal trajectory. Figure 8 purposely illustrates various smoothing teaching trajectories that progressively approach the original therapist's reference trajectory, represented by the continuous line, underscoring the flexibility and efficacy of this approach.

Indeed, it's important to note that both κ_τ and κ_s are coefficients specific to each exercise trajectory, differences of patient's limbs size or patient's motion conditions. The coefficients are manually adjusted individually for different exercises based on the patient's comfort. This adaptability ensures that the smoothing coefficients are tailored to the characteristics of each exercise, optimising their effectiveness.
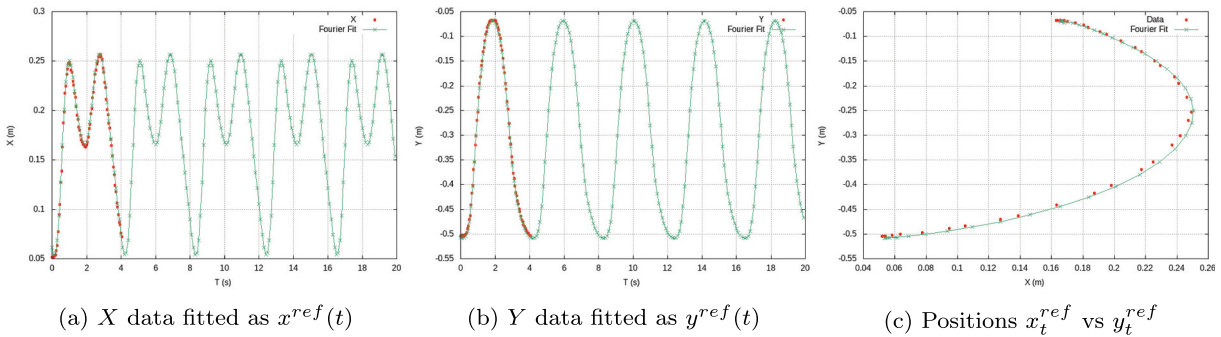
3. Rehabilitation trajectory model

From the perspective of the patient-exoskeleton interface, the instructional trajectory $\mathcal{S}$ is inherently expressed in polar form. To facilitate processing, it is subsequently transformed into Cartesian points at the wrist location, represented as $x_i^{ref} = \ell_1 \cos(\theta_1) + \ell_2 \cos(\theta_1 + \theta_2)$ and $y_i^{ref} = \ell_1 \sin(\theta_1) + \ell_2 \sin(\theta_1 + \theta_2)$, commonly referred to as the ideal or reference trajectory $\mathbf{p}^{ref}$. In lieu of managing an extensive dataset comprising hundreds or thousands of points, this study derives an adaptive analytical reference model expressed as functions of time, akin to the approach proposed by Arteaga et al. (2020). Given the periodic nature of a rehabilitation exercise assumed to be a Cartesian function, the suggested methodology involves obtaining xx and yy separately with respect to time. The utilization of a general Fourier series is deemed apt for representing a suitable function of time, providing a concise and analytically manageable characterisation of the patient's movement trajectory.

(a) Reference scaled only.

(b) Reference scaled and translated.

Figure 8. Family of smoothed reference trajectories adjusted by κ_τ and κ_s.

(a) X data fitted as $x^{ref}(t)$

(b) Y data fitted as $y^{ref}(t)$

(c) Positions x_t^{ref} vs y_t^{ref}

Figure 9. Periodic positions of shoulder flexion-extension fitted by fourier series.

$$x(t) = \alpha_0^x + \alpha_k^x \cos(k\omega t) + \beta_k^x \sin(k\omega t) + \dots \quad (17a)$$

and

$$y(t) = \alpha_0 + \alpha_k^y \cos(k\omega t) + \beta_k^y \sin(k\omega t) + \dots \quad (17b)$$

In the general formulation (18)-(20) the Fourier series estimate the coefficients for (17). The parameter n represents the number of data to be fitted through the Fourier series. However, the k_{th} number of Fourier coefficients are predetermined with a sufficiently large value to appropriately accommodate the trajectory data. Equations 18, 19, and 20 comprise the Fourier series tailored to fit the trajectory data provided by the therapist, expressing it as a trigonometric function.

A C++ program was implemented to autonomously compute the discrete Fourier coefficients. Regarding the independent terms, the average of the discrete data is presented as follows:

$$\alpha_0^x = \frac{1}{n}\sum_{k=1}^{n} x_k, \quad \text{and} \quad \alpha_0^y = \frac{1}{n}\sum_{k=1}^{n} y_k. \quad (18)$$

Similarly, even though initially presented in continuous-time, the discrete Fourier series was formulated to derive the remaining coefficients for the Cartesian component x vs t by

$$\alpha_k^x = \frac{2}{n}\int_t x(t)\cos(k\omega t)\mathrm{d}t, \quad \beta_k^x = \frac{2}{n}\int_t x(t)\sin(k\omega t)\mathrm{d}t \quad (19)$$

likewise, for the Cartesian component y vs t

$$\alpha_k^y = \frac{2}{n}\int_t y(t)\cos(k\omega t)\mathrm{d}t, \quad \beta_k^y = \frac{2}{n}\int_t y(t)\sin(k\omega t)\mathrm{d}t. \quad (20)$$

Therefore, we have now acquired the Cartesian components of an xy trajectory as reference functions of time, denoted as $x(t)$ and $y(t)$. The numerical coefficients related to time obtained to align with the experimental reference data of shoulder flexion-extension, illustrated in Figure 9, are:

$$\begin{aligned} x_t^{ref} = 0.17 - 0.05\cos(\omega t) - 0.06\cos(2\omega t) \\ + 0.01(\sin(2\omega t) - \sin(3\omega t)) \end{aligned} \quad (21)$$

and

$$\begin{aligned} y_t^{ref} = -0.30 - 0.22\cos(\omega t) + 0.05\sin(\omega t) - 0.02\sin(2\omega t) \\ + 0.01(\cos(3\omega t) - \sin(3\omega t)). \end{aligned}$$
$$(22)$$

The experimental coefficients obtained are presented for illustrative purposes, specifically related to Figure 9. It's essential to note that their numeric values may vary for different exercises or when administered by a human therapist, accounting for differences in limb size.

3.1. EMG sensing model calibration

This study suggests deriving a sensing model for estimating the Cartesian position of the limb through EMG measurements. Given the challenge of achieving repeatability in EMG data from the same exercises and subjects, an EMG calibration model is established at the onset of training. Real-time motion prediction becomes feasible using raw EMG data, typically encompassing combined muscle motions (Alenabi et al. 2013). Table 2 provides a comprehensive overview, detailing the type of therapy and the associated muscles involved in obtaining EMG measurements.

Based on the electrodes illustrated in Figure 10c, the experimental raw EMG data is presented in Figure 14. This data pertains to the shoulder-elbow-wrist region and corresponds to multiple periodic flexion-extension exercises.

The series of plots illustrated in Figure 11 portrays three distinct experiments involving the same exercise, specifically elbow flexions, each comprising approximately five repetitions. In this configuration, Channel Ch5 was situated at the *bicep brachii* muscle, while concurrently, Channel Ch6 was positioned at the *tricep brachial* muscle. Notably, the magnitudes of amplitude (μV) exhibit coherence and consistency across both channels.

The subsequent Figure 12 illustrates an experiment involving shoulder flexion. In this instance, Channel Ch5 was positioned at the *Pectoralis Major* muscle, and Channel Ch6 was situated at the *Deltoid Anterior* muscle. The plots represent approximately five oscillations (flexions) with amplitude magnitudes measured in μV. It is noteworthy that, in this case, both frequency and amplitudes consistently differ from those observed in other exercises.

Figure 13 presents experimental data related to rowing-like movements, showcasing three distinct experiments involving the same exercise with approximately six rowing flexions each. Channel Ch5 was positioned at the *Trapezius middle* muscle, while Channel Ch6 was situated at the *Deltoid anterior* muscle. The amplitude magnitudes (μV) and oscillation frequency

exhibit distinct behavioral patterns, maintaining substantial consistency across both channels.

The activity level of muscles is inherently noisy due to the interaction of bi-joint muscles with movements in other joints. The EMG calibration measurement is acquired by initially filtering the noisy native EMG signal $\tilde{E}$ (Figure 14) into a linear envelope $\bar{E}_t$ within segments of N_k samples. Subsequently, a 2nd order low-pass filter with a cutoff frequency $f_c = 20Hz$ is applied,

$$\bar{E}_t = \left| \tilde{E} - \frac{1}{N_k} \sum_{1}^{N_k} \tilde{E}_i \right|, \quad E_t^{cal} = \frac{\bar{E}_t}{\sqrt[2]{1 + \left(\frac{f_t}{f_c}\right)^4}}. \quad (23)$$

Consequently, an instantaneous EMG calibration measurement value, denoted as E_t^{cal}, is deduced from the periodicity of the filtered EMG signal $\bar{E}_t$. To obtain an analytical representation of E^{cal} over a period of a specified exercise, a fitness model employing a *Fourier* series in terms of time, denoted as E_t^{cal}, is derived.

$$\begin{aligned} E_t^{cal} = {}& 56.60 - 29.65\cos(\omega t) - 15.53\sin(\omega t) - 2.18\cos(2\omega t) \\ & + 7.73\sin(2\omega t) - 1.37\cos(3\omega t) + 0.13\cos(5\omega t) \\ & + 2.58\sin(5\omega t). \end{aligned} \quad (24)$$

The numerical coefficients in (24) are derived from the experimental shoulder-elbow flexion-extension exercise shown in Figure 14. Let's introduce a polynomial function $\hat{E}(t)$ as a time-dependent function capable of estimating EMG measurements over time. This function can then be compared against the calibrated model E_t^{cal}, which serves as a reference function over time. To approximate E_t^{cal}, we employ the Taylor series (Maclaurin), representing it as $\hat{E}(t)$.

$$\hat{E}(t) \approx \frac{E_0^{(0)}}{0!}t^0 + \frac{E_0^{(1)}}{1!}t + \frac{E_0^{(2)}}{2}t^2 + \cdots \frac{E_0^{(m)}}{m!}t^m. \quad (25)$$

A polynomial approximation is advantageous for an observer due to its simplicity in terms of differentiation and integration

Table 2. EMG electrodes placement for different therapy.

Exercise[a]	Channel 1	Channel 2
Elbow	Biceps brachii	Triceps brachii
Shoulder	Pectoralis major	Anterior pectoralis
Shoulder and elbow	Middle trapezius	Anterior deltoid
Knee	Rectur femoris	Vastus medialis

[a]Flexion-extension exercise. See Figure 10 for channels placement.
MOBIlab+ sampling 256Hz, high/low pass filters 100/0.5Hz.

(a) Elbow electrodes.　　　(b) Shoulder electrodes.　　　(c) Shoulder-elbow electrodes.
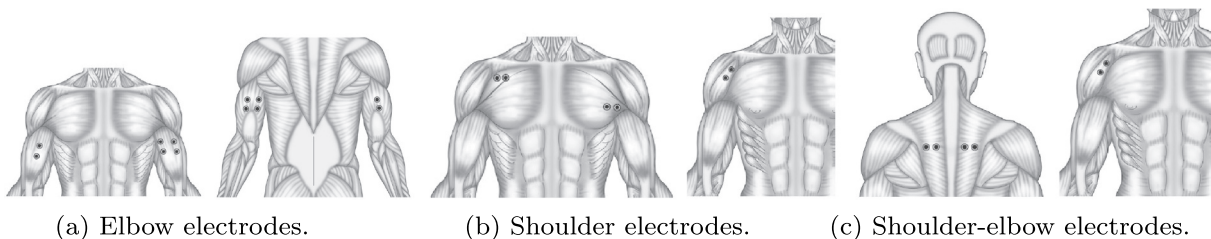
Figure 10. The upper limbs' EMG electrode placement is delineated in channel 1 (left) and channel 2 (right).
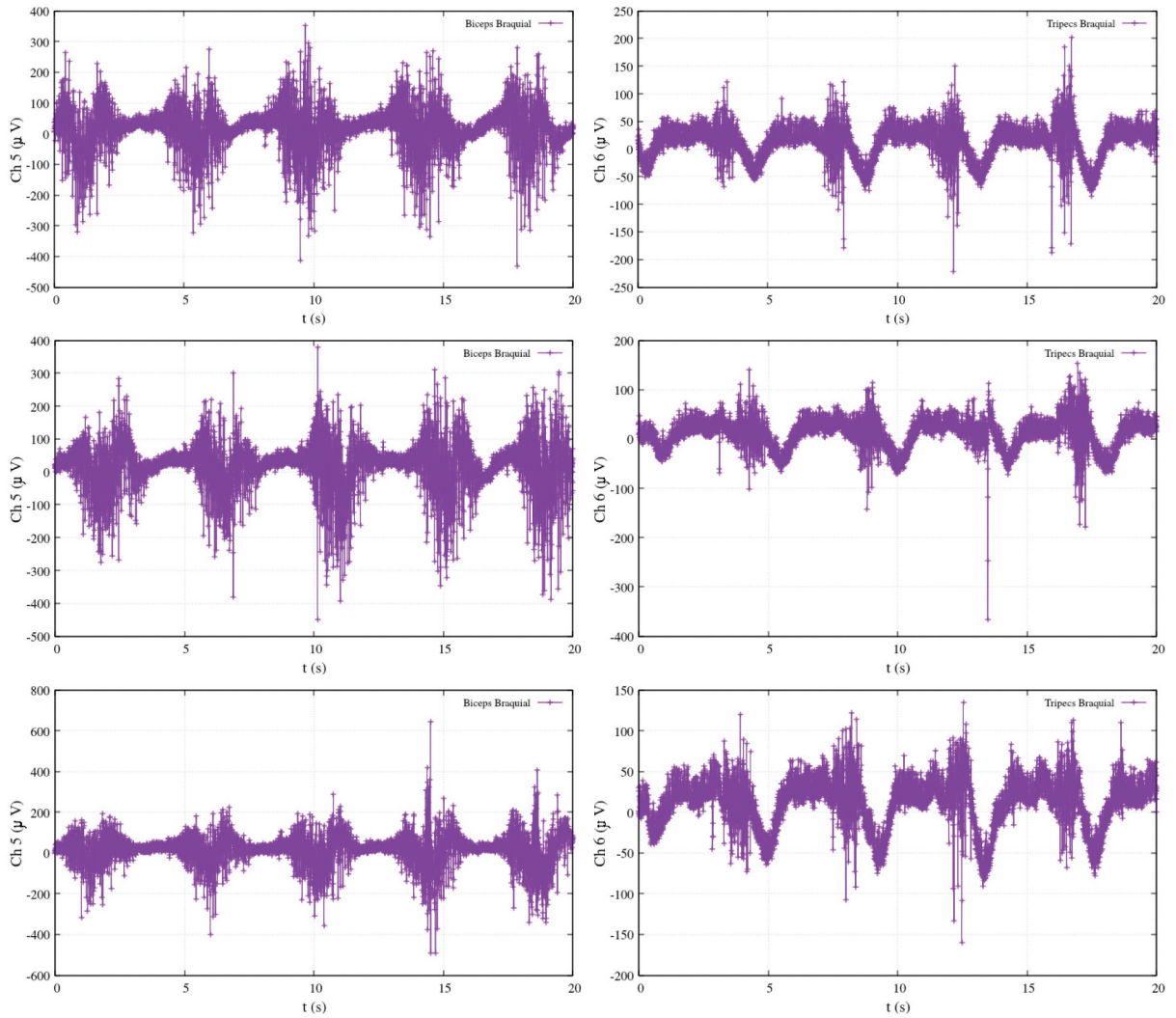
Figure 11. Three elbow-flexion EMG measurements. Channels are Ch5 (*bicep braquial*) and Ch6 (*tricep braquial*).
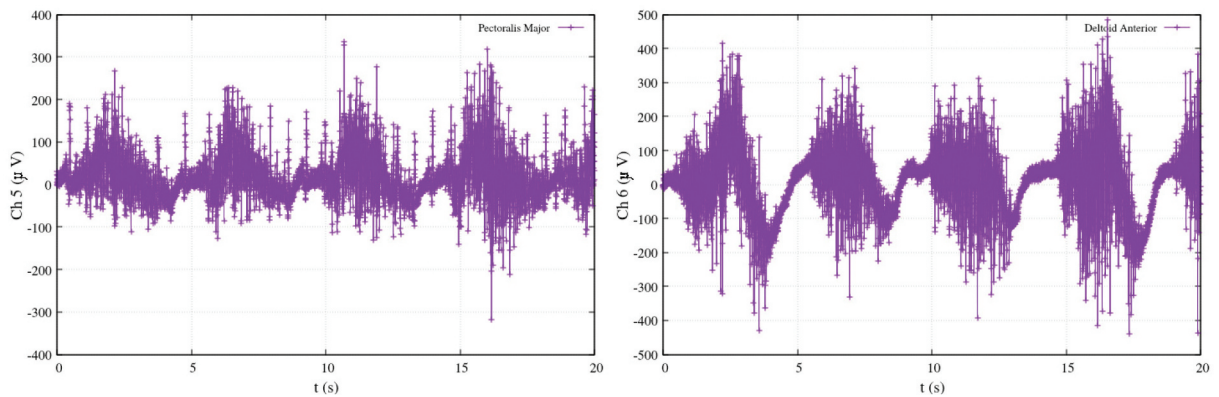

Figure 12. Shoulder flexion EMG measurements. Channels Ch5 are (*Pectoralis Major*) and Ch6 (*Deltoid Anterior*).

with respect to time. In Figure 15a, a gradual polynomial fitting up to the 80th degree aligns with our calibration model (24). Additionally, Figure 15b visually represents the correlation between raw EMG data, overlaid with calibrated signals (filtered out), and their corresponding Cartesian positions over time during periodic exercises.

3.2. Observability based on real-time EMG

Given that the polynomial observation model $\hat{E}(t)$ is expressed as a function of time t, its inverse model $t(\hat{E}_t)$ provides a time value consistent with representing instantaneous Cartesian positions $x(t)$ and $y(t)$. In the case of the experimental EMG
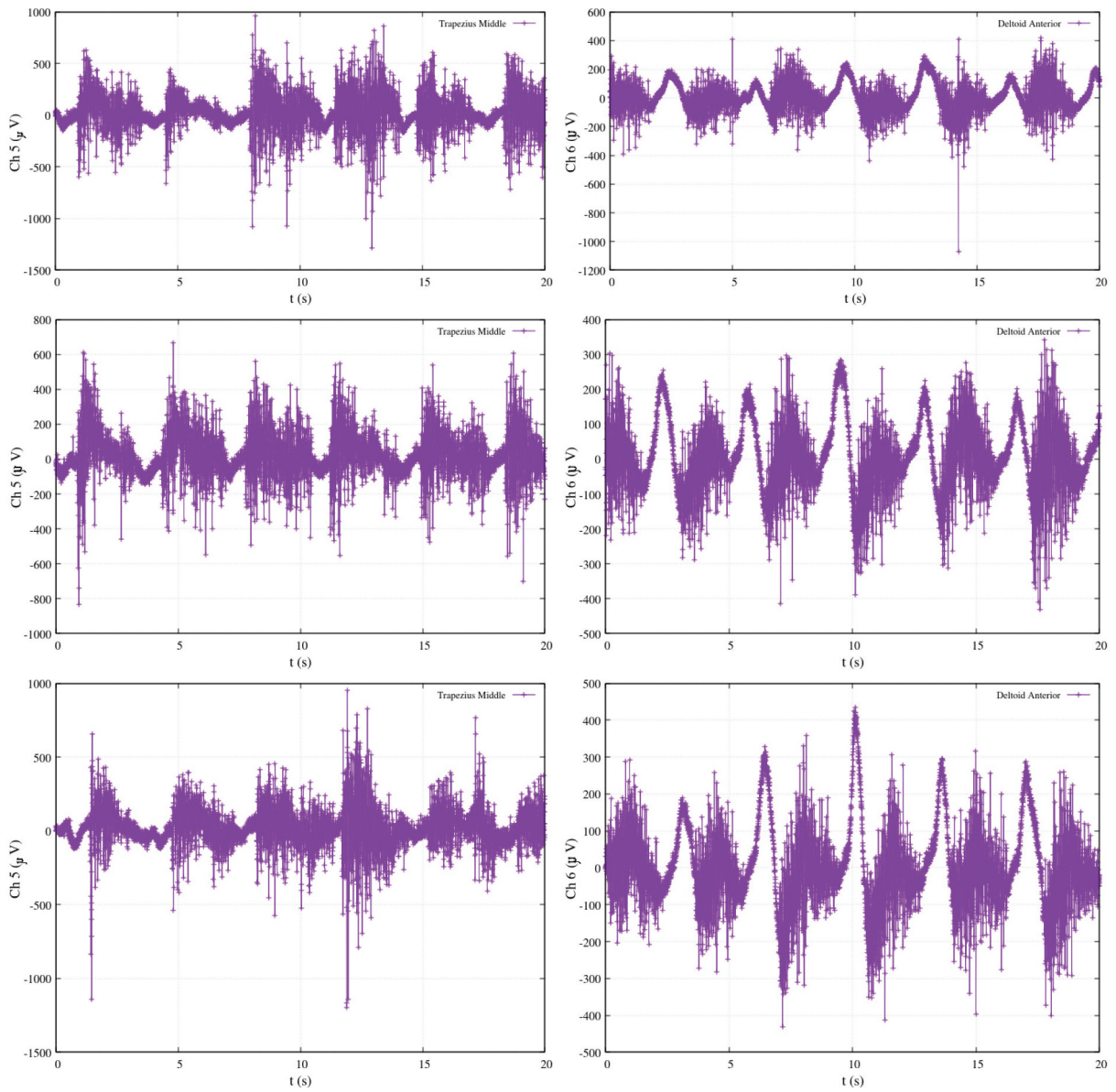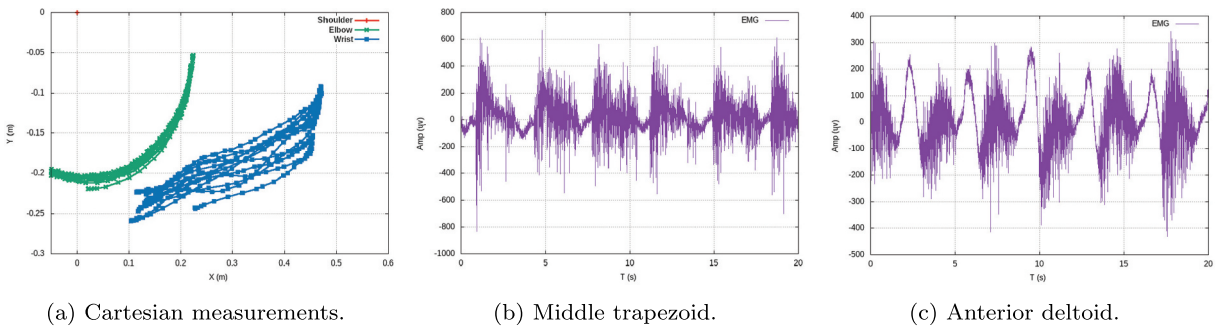
Figure 13. Three different experiments of rowing exercise using EMG channels Ch5 (*Trapezius middle*) and Ch6 (*Deltoid anterior*).

(a) Cartesian measurements. (b) Middle trapezoid. (c) Anterior deltoid.

Figure 14. Native EMG signals $\tilde{E}$ during simultaneous shoulder-elbow flexion extension and wrist.

data from Figure 16, an 80th grade polynomial was obtained. As obtaining a non-linear analytical solution is not trivial, its inverse result for time is numerically calculated through the Newton-Raphson method for nonlinear equations. The instantaneous measurement $\hat{E}_t$ substitutes the left side of the following expression,

$$\hat{E}(t) = a_0 + a_1\hat{E} + a_2\hat{E}^2 + a_3\hat{E}^3 + \ldots + a_i\hat{E}^i \qquad (26)$$

where the time t_k is the unknown value. Therefore, the Newton-Raphson method necessitates the first-order derivative with respect to time $d\hat{E}/dt$,

$$\hat{E}(t) = \frac{d\hat{E}(t)}{dt} = a_1 + a_2\hat{E}_t + 2a_3\hat{E}_t^2 + \ldots + a_i(i-1)\hat{E}_t^{i-1} \quad (27)$$

hence, a solution for t_k is provided in the following manner,

$$\hat{t}_k = \hat{t}_{k-1} - \frac{\hat{E}(t)}{\hat{\hat{E}}(t)}, \quad (28)$$

recursively, the best solution approximation is iteratively refined until the relative numeric error falls below ε_t.

$$\left| \frac{\hat{t}_k - \hat{t}_{k-1}}{\hat{t}_k} \right| < \varepsilon_t \quad (29)$$

and now Cartesian models are satisfied as a functions of time t_k as well

$$\hat{x}(\hat{t}) = b_0 + b_1\hat{t} + b_2\hat{t}^2 + \ldots + b_i\hat{t}^i, \quad (30)$$

$$\hat{y}(\hat{t}) = c_0 + c_1\hat{t} + c_2\hat{t}^2 + \ldots + c_i\hat{t}^i. \quad (31)$$

The solution for t_k establishes synchronicity between $\hat{E}_t$ and the expected Cartesian positions (x_t^{ref}, y_t^{ref}) in (21) and (22), respectively. Figures 16a,b display the native data and filtered signals for two EMG channels. Similarly, Figure 16c presents only the filtered signals.

4. Exoskeletons morphology and control law

In this study, a proposed exoskeleton model incorporates a well-designed mechanism to facilitate standard rehabilitation exercises (Figure 18). Alternative methodologies, such as adaptive geometrical design, have been documented in previous literature (Wang et al. 2014) and locomotive control strategies (Goh Haoyong Yu et al., 2006). The design of speed reducers (e.g. the shoulder mechanism shown in Figure 17a) primarily incorporates pulse encoders for joint rotation sensing. These mechanisms are intended to enforce limb tracking along the reference trajectories.

The design assumes all encoders have a constant angular resolution R [pulses/rev]. The number of pulses η_t measures the motor's instantaneous angle θ_0 [rad], and its angular speed w_0 [rad/s].
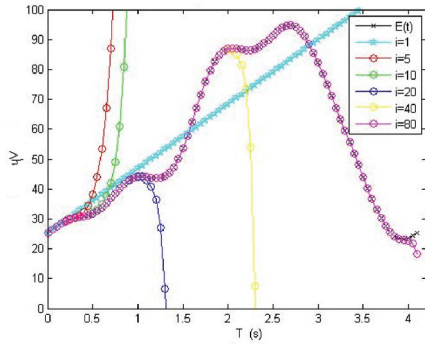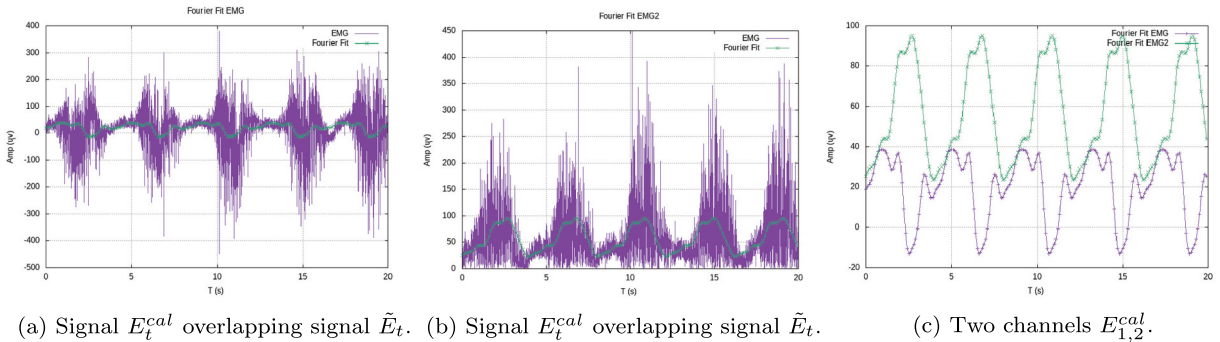

(a) Multiple approximations.
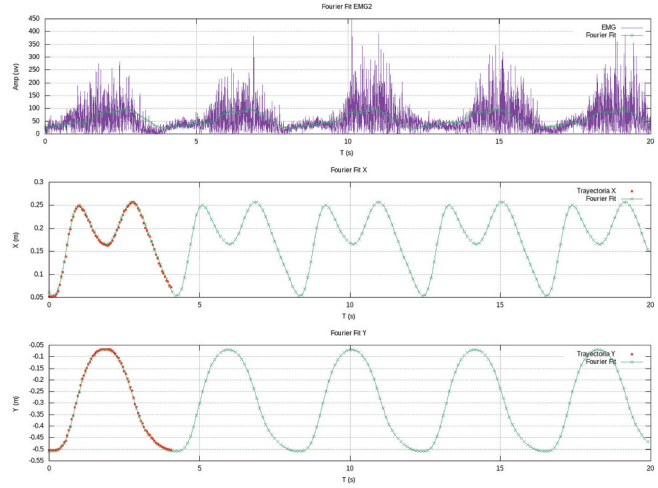
(b) EMG singnals with respective XY fitting.

Figure 15. $E(t)$ polynomial fitting with i^{th} coefficients by McLaurin series.

(a) Signal E_t^{cal} overlapping signal $\tilde{E}_t$.   (b) Signal E_t^{cal} overlapping signal $\tilde{E}_t$.   (c) Two channels $E_{1,2}^{cal}$.

Figure 16. Shoulder flexion-extension EMG measurement.

$$\theta_0 = \frac{2\pi}{R}\eta_t, \quad w_0 = \frac{2\pi}{R}\left(\frac{\eta_{t_2} - \eta_{t_1}}{t_2 - t_1}\right). \qquad (32)$$

All gears' rotary speeds are described by (33) and illustrated in Figure 17b. Gears with a radius r_i yield speeds w_i as functions of the motor's velocity w_0,

$$\begin{pmatrix} w_1 \\ w_{23} \\ w_5 \\ w_7 \\ w_8 \end{pmatrix} = w_0 \begin{pmatrix} \frac{r_0}{r_1} \\ \frac{r_0}{r_1} \\ \frac{r_0 r_{23}}{r_1 r_5} \\ \frac{r_0 r_{23}}{r_1 r_5} \\ \frac{r_0 r_{23} r_7}{r_1 r_5 r_8} \end{pmatrix}. \qquad (33)$$

By expressing (33) in vector notation, the time-invariant linear system (34) emerges,

$$\mathbf{w} = w_0 \mathbf{k}. \qquad (34)$$

This model encapsulates the functional representation of the joints, providing a framework to deduce Cartesian positions over time for feedback purposes. In Figure 18, the kinematic parameters of the upper and lower limbs are illustrated, featuring a structured organisation of joint axes. In addition, Table 3 shows the physics-based parameters used for computer simulations.

Therefore, it follows a dynamic controller at the level of the exoskeleton's joint gearing, rather than at the level of the limbs' global kinematic-EMG calibration. Employing an Euler-Lagrange approach, the general Lagrangian model $\mathcal{L}_i$ for the ith gear, transmitting rotary kinetic and potential energy, is:

$$\mathcal{L}_i = r_i^2 m_i \dot{\phi}_i - m_i g r_i \sin(\phi_i), \qquad (35)$$

and developing the following differential equation

$$\tau_i = \frac{d}{dt}\left(\frac{d\mathcal{L}}{d\dot{\phi}_i}\right) - \frac{d\mathcal{L}}{d\phi_i}. \qquad (36)$$

Subsequently, by considering and substituting joint kinematics from (34), and simplifying in terms of controlled motor motion ϕ_0, the following dynamic vector $\tau = (\tau_1, \tau_{23}, \tau_5, \tau_7, \tau_8)^{\mathsf{T}}$ is deduced,

$$\tau = \begin{pmatrix} r_0 r_1 m_1 \ddot{\phi}_0 + m_1 g r_1 \cos\left(\frac{r_0}{r_1}\phi_0\right) \\ \frac{r_{23}^2 r_0}{r_1} m_{23} \ddot{\phi}_0 + m_{23} g r_{23} \cos\left(\frac{r_0}{r_1}\phi_0\right) \\ \frac{r_0 r_{23} r_5}{r_1} m_5 \ddot{\phi}_0 + m_5 g r_5 \cos\left(\frac{r_0 r_{23}}{r_1 r_5}\phi_0\right) \\ \frac{r_0 r_{23} r_7^2}{r_1 r_5} m_7 \ddot{\phi}_0 + m_7 g r_7 \cos\left(\frac{r_0 r_{23}}{r_1 r_5}\phi_0\right) \\ \frac{r_0 r_{23} r_7 r_8}{r_1 r_5} m_8 \ddot{\phi}_0 + m_8 g r_8 \cos\left(\frac{r_0 r_{23} r_7}{r_1 r_5}\phi_0\right) \end{pmatrix}. \qquad (37)$$
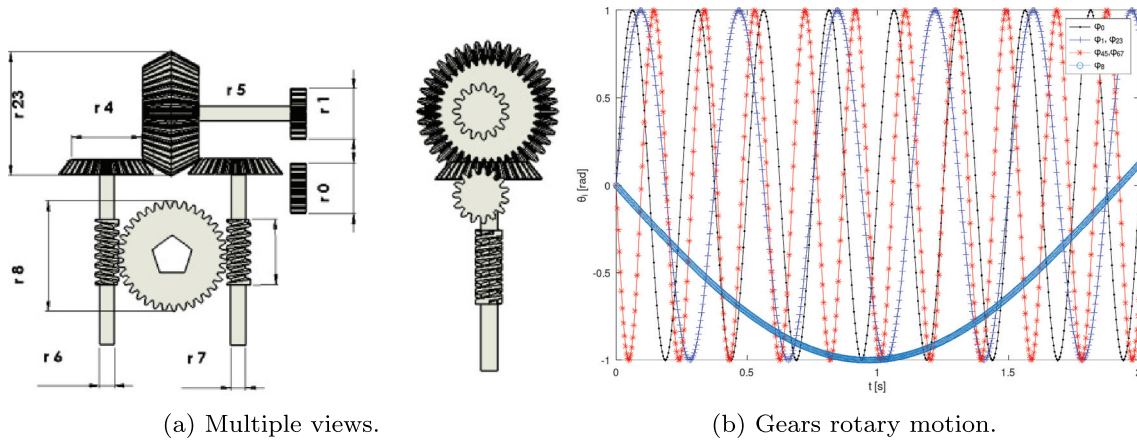

(a) Multiple views.

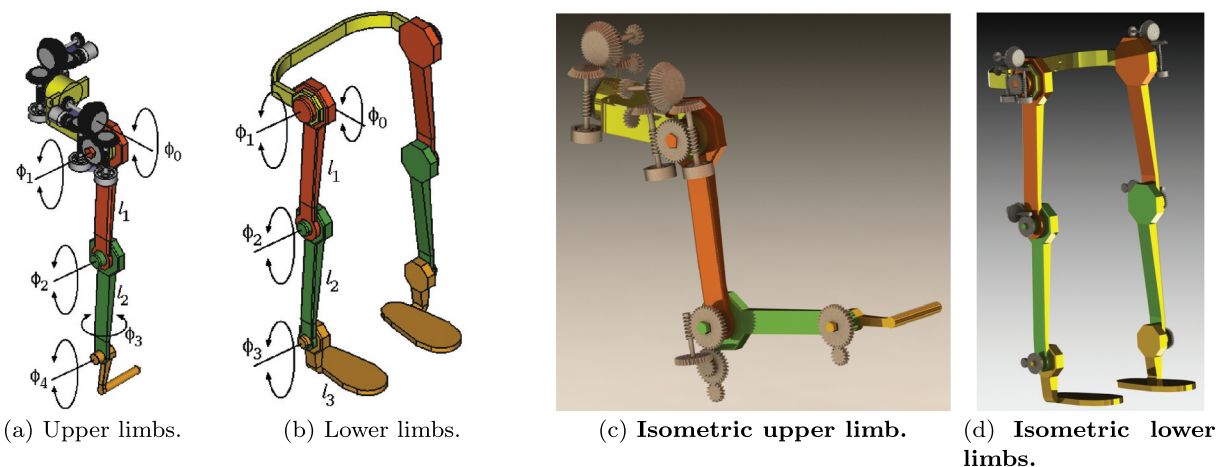(b) Gears rotary motion.

Figure 17. The joint's mechanism.

(a) Upper limbs.   (b) Lower limbs.   (c) **Isometric upper limb.**   (d) **Isometric lower limbs.**

Figure 18. Exoskeleton mechanism structure.

Table 3. Physics-based computer simulation parameters[a].

Limbs:			
$m = 1$ kg	$l_x = 0.1666$ kg m^2	$l_y = 0.1666$ kg m^2	$l_z = 0.1666$ kg m^2
$l_{1,2} = 0.3$ m	limbs $r_{1,2} = 0.15$ m	$\tau_{ref} = 19.62$ Nm	$\ddot{\phi}_{ref} = 36.14$ s^{-2}
Gears:			
$r_1 = 1.5r_0$ m	$r_{2,3} = 2.6r_0$ m	$r_{4,5} = 2r_0$ m	$r_{6,7} = 0.66r_0$ m
$r_8 = 1.16r_0$ m	$n_{6,7} = 2$ (threads)	$n_8 = 40$ (teeth)	$m_8 = 1.166m_0$ kg
$m_1 = 1.5m_0$ kg	$m_{2,3} = 3m_0$ kg	$m_{4,5} = 2m_0$ kg	$m_{6,7} = 1.5m_0$ kg
$l_1 = 3.37r_0^2 m_0$ kg m^2	$l_{2,3} = 1.72r_0^2 m_0$ kg m^2	$l_{4,5} = 8r_0^2 m_0$ kg m^2	$l_{6,7} = 0.2875r_0^2 m_0$ kg m^2
$l_8 = 1.58r_0^2 m_0$ kg m^2			

[a]Gazebo enabled with Object Dynamic Object (ODE).

Expressing τ in terms of the explicit vectors for inertia **m** and gravity force **g**,

$$\tau = \begin{pmatrix} r_0 r_1 m_1 \ddot{\phi}_0 \\ \frac{r_{23}^2 r_0}{r_1} m_{23} \\ \frac{r_0 r_{23} r_5}{r_1} m_5 \\ \frac{r_0 r_{23} r_7^2}{r_1 r_5} m_7 \\ \frac{r_0 r_{23} r_7 r_8}{r_1 r_5} m_8 \end{pmatrix} \ddot{\phi}_0 + \begin{pmatrix} m_1 g r_1 \cos\left(\frac{r_0}{r_1}\phi_0\right) \\ m_{23} g r_{23} \cos\left(\frac{r_0}{r_1}\phi_0\right) \\ m_5 g r_5 \cos\left(\frac{r_0 r_{23}}{r_1 r_5}\phi_0\right) \\ m_7 g r_7 \cos\left(\frac{r_0 r_{23}}{r_1 r_5}\phi_0\right) \\ m_8 g r_8 \cos\left(\frac{r_0 r_{23} r_7}{r_1 r_5}\phi_0\right) \end{pmatrix} \quad (38)$$

and expressing this relationship in vector notation, the following dynamic equation is formulated,

$$\tau = \mathbf{m}\ddot{\phi}_0 + \mathbf{g}(\phi_0). \quad (39)$$

It follows that a controller is deduced from the dynamic Equation (39). Thus, rewriting the torque vector with a differential equation notation,

$$\tau = \mathbf{m}\frac{d\dot{\phi}}{dt} + \mathbf{g}(\phi_0) \quad (40)$$

and by separating different differentials,

$$(\tau - \mathbf{g}(\phi_0))dt = \mathbf{m}d\dot{\phi}_0 \quad (41)$$

solving by definite integration,

$$(\tau - \mathbf{g}(\phi_0))\int_{t_2}^{t_1} dt = \mathbf{m}\int_{\phi_1}^{\phi_2} d\dot{\phi}_0, \quad (42)$$

then by algebraically arranging and changing subindex notation, a model-based controller is yielded

$$\dot{\phi}_{0_{t+1}} = \dot{\phi}_{0_t} + \mathbf{m}^+\left(\tau^{ref} - \mathbf{g}(\phi_0)\right)(t_2 - t_1), \quad (43)$$

where $\mathbf{m}^+$ is the inertia vector pseudoinverse.[2] Thus, the speeds of the exoskeleton's joint mechanisms are recursively controlled according to a specified reference torque τ^{ref}.

4.1. Limbs kinematic model

Based on the mechanical model presented in Figure 18, a set of Cartesian equations was deduced for kinematic analysis, forming the foundation for position control. The non-linear and non-square systems obtained in (44) and (45) evidently lack inverse analytical solutions. Therefore, an algebraic numeric recursive approach was developed. Expressions (44a)-(44c) describes the upper limb kinematics of the 5 rotary joints. Notice that ϕ_0 and ϕ_3 are rolling axis. Thus, for x,

$$x = l_1 s_1 + l_2 s_{12} + l_3 s_3 s_{123}, \quad (44a)$$

for coordiante y

$$y = -s_0(l_1 s_1 + l_2 s_{12} + l_3 s_{124}) + l_3 s_3 s_{124} s_0 \quad (44b)$$

and for coordinate z,

$$z = -s_0(l_1 s_1 + l_2 s_{12} + l_3 s_{124}) - l_3 s_3 s_{124} s_0. \quad (44c)$$

Expressions (45a)-(45c) are the kinematic equations of the lower limb with 4 rotary joints,

$$x = l_1 s_1 + l_2 s_{12} + l_3 s_{123} \quad (45a)$$

and

$$y = -s_0(l_1 s_1 + l_2 s_{12} - l_3 s_{123}) \quad (45b)$$

and

$$z = -s_0(l_1 s_1 + l_2 s_{12} - l_3 s_{123}). \quad (45c)$$

The instantaneous *Jacobian* matrix represents the rate of change of coordinates *xyz* w.r.t. the joint-space vector $\mathbf{\Phi} = (\phi_0, \phi_1, \phi_2, \dots \phi_n)^{\mathsf{T}}$ of length n. Such that,

$$\mathbf{J}(\mathbf{\Phi}) = \begin{pmatrix} \frac{\partial x}{\partial \phi_0} & \frac{\partial x}{\partial \phi_1} & \frac{\partial x}{\partial \phi_2} & \cdots & \frac{\partial x}{\partial \phi_n} \\ \frac{\partial y}{\partial \phi_0} & \frac{\partial y}{\partial \phi_1} & \frac{\partial y}{\partial \phi_2} & \cdots & \frac{\partial y}{\partial \phi_n} \\ \frac{\partial z}{\partial \phi_0} & \frac{\partial z}{\partial \phi_1} & \frac{\partial z}{\partial \phi_2} & \cdots & \frac{\partial z}{\partial \phi_n} \end{pmatrix}. \quad (46)$$

For the upper limb the *Jacobian* matrix elements are

$$\frac{\partial x}{\partial \phi_0} = 0 \quad (47)$$

$$\frac{\partial x}{\partial \phi_1} = l_1 s_1 + l_2 s_{12} + l_3 s_3 s_{124} \quad (48)$$

$$\frac{\partial x}{\partial \phi_2} = l_2 s_{12} + l_3 s_3 s_{124} \quad (49)$$

$$\frac{\partial x}{\partial \phi_3} = -l_3 s_3 s_{124} \quad (50)$$

$$\frac{\partial x}{\partial \phi_4} = l_3 s_3 s_{124}, \quad (51)$$

and for y,

$$\frac{\partial y}{\partial \phi_0} = s_0(l_1 s_1 + l_2 s_{12} + l_3 s_{124}) + l_3 s_3 s_{124} s_0 \quad (52)$$

$$\frac{\partial y}{\partial \phi_1} = s_0(l_1 s_1 + l_2 s_{12} + l_3 s_{124}) + l_3 s_3 s_{124} s_0 \qquad (53)$$

$$\frac{\partial y}{\partial \phi_4} = l_3 s_{124} s_0 + l_3 s_3 s_{124} s_0, \qquad (56)$$

and for z,

$$\frac{\partial y}{\partial \phi_2} = s_0(l_2 s_{12} + l_3 s_{124}) + l_3 s_3 s_{124} s_0 \qquad (54)$$

$$\frac{\partial z}{\partial \phi_0} = -s_0(l_1 s_1 + l_2 s_{12} + l_3 s_{124}) + l_3 s_3 s_{124} s_0 \qquad (57)$$

$$\frac{\partial y}{\partial \phi_3} = l_3 s_3 s_{124} s_0 \qquad (55)$$

$$\frac{\partial z}{\partial \phi_1} = s_0(l_1 s_1 + l_2 s_{12} + l_2 s_{12} + l_3 s_{124}) - l_3 s_3 s_{124} s_0 \qquad (58)$$
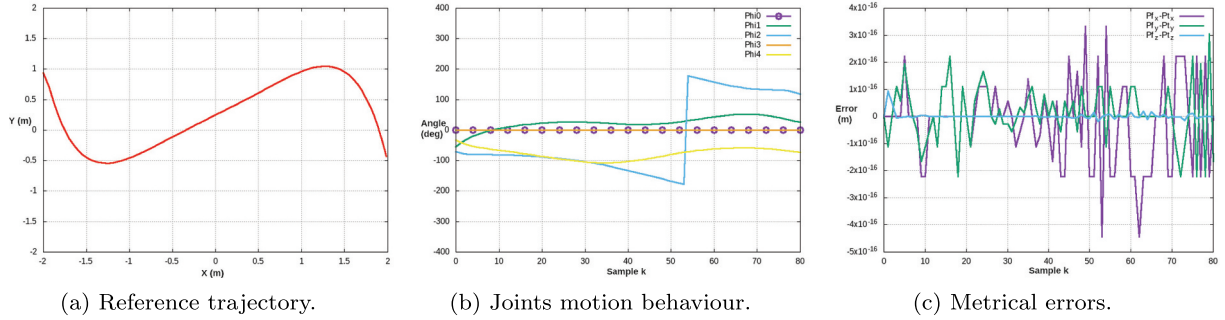

(a) Reference trajectory.   (b) Joints motion behaviour.   (c) Metrical errors.

Figure 19. Tracking control of a complex reference trajectory.
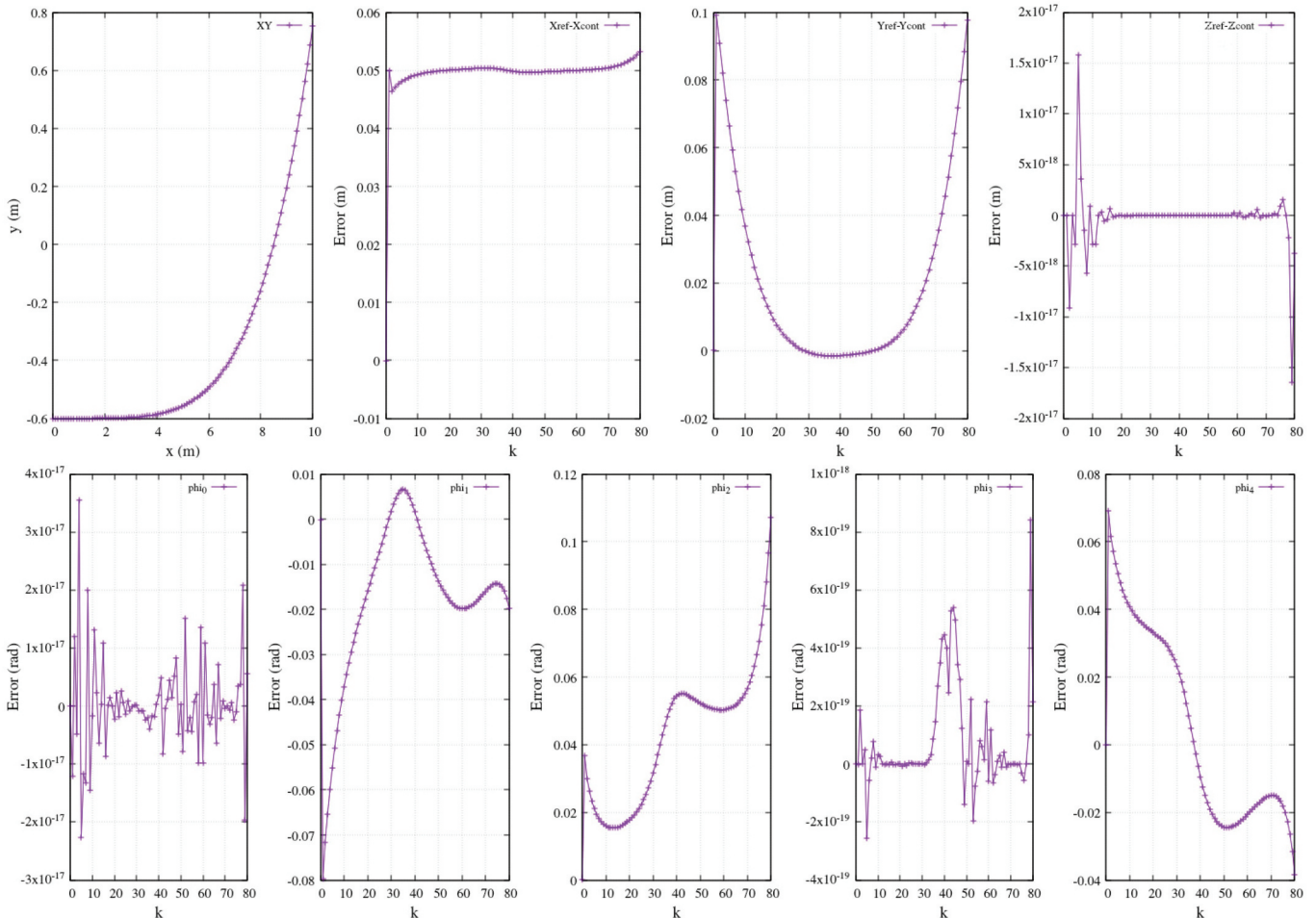

Figure 20. Trajectory tracking metric errors, reference $\mathbf{p}^{ref} - \mathbf{p}_t$, tracking $y(x) = k_5 x^5 + k_3 x^3 - k_0$ and joints' error.

$$\frac{\partial z}{\partial \phi_2} = s_0(l_2 s_{12} + l_3 s_{124}) - l_3 s_3 s_{124} s_0 \tag{59}$$

$$\frac{\partial z}{\partial \phi_3} = -l_3 s_3 s_{124} s_0 \tag{60}$$

$$\frac{\partial z}{\partial \phi_4} = l_3 s_{124} s_0 - l_3 s_3 s_{124} s_0 \tag{61}$$

Likewise, for the lower limb, the *Jacobian* matrix terms are

$$\frac{\partial x}{\partial \phi_0} = 0; \quad \frac{\partial x}{\partial \phi_1} = l_1 s_1 + l_2 s_{12} - l_3 s_{123}; \tag{62}$$

$$\frac{\partial x}{\partial \phi_2} = l_2 s_{12} - l_3 s_{123}; \quad \frac{\partial x}{\partial \phi_3} = -l_3 s_{123}. \tag{63}$$

and for *y*

$$\frac{\partial y}{\partial \phi_0} = s_0(l_1 s_1 + l_2 s_{12} - l_3 s_{123}) \tag{64}$$

$$\frac{\partial y}{\partial \phi_1} = s_0(l_1 s_1 + l_2 s_{12} + l_3 s_{123}) \tag{65}$$

$$\frac{\partial y}{\partial \phi_2} = s_0(l_2 s_{12} + l_3 s_{123}); \quad \frac{\partial y}{\partial \phi_3} = l_3 s_0 s_{123}. \tag{66}$$

and for *z*

$$\frac{\partial z}{\partial \phi_0} = -s_0(l_1 s_1 + l_2 s_{12} - l_3 s_{123}) \tag{67}$$

$$\frac{\partial z}{\partial \phi_1} = s_0(l_1 s_1 + l_2 s_{12} + l_3 s_{123}) \tag{68}$$

$$\frac{\partial z}{\partial \phi_2} = s_0(l_2 s_{12} + l_3 s_{123}); \quad \frac{\partial z}{\partial \phi_3} = l_3 s_0 s_{123} \tag{69}$$

4.2. Recursive time-variant control law

Other exoskeleton control approaches have addressed nonlinearity using sliding surfaces Zhu et al. (2016) or adaptive methods, implementing impedance with feedback using biosignals Li et al. (2017), and neural approximation He et al. (2019).

The present work takes an approach involving a model-based algebraic linear recursive system of equations. This work deduces a time-variant redundant kinematics controller since $\mathbf{J}_t$ is considered. The model incorporates the reference trajectory provided by the therapist, denoted as $\mathbf{p}^{ref}$. The real-time feedback utilises the EMG observation $\hat{\mathbf{p}}_t = (\hat{x}_t, \hat{y}_t)^\mathsf{T}$. The innovation model, representing the local reference, is the inverse model $\boldsymbol{\Phi}_{t+1}$, and the updating model involves the encoders' observation $\dot{\boldsymbol{\Phi}}_t$.

Let us define the state linear Equation (75) as the first-order derivative forward kinematics.

$$\dot{\mathbf{p}} = \mathbf{J} \cdot \dot{\boldsymbol{\Phi}}$$
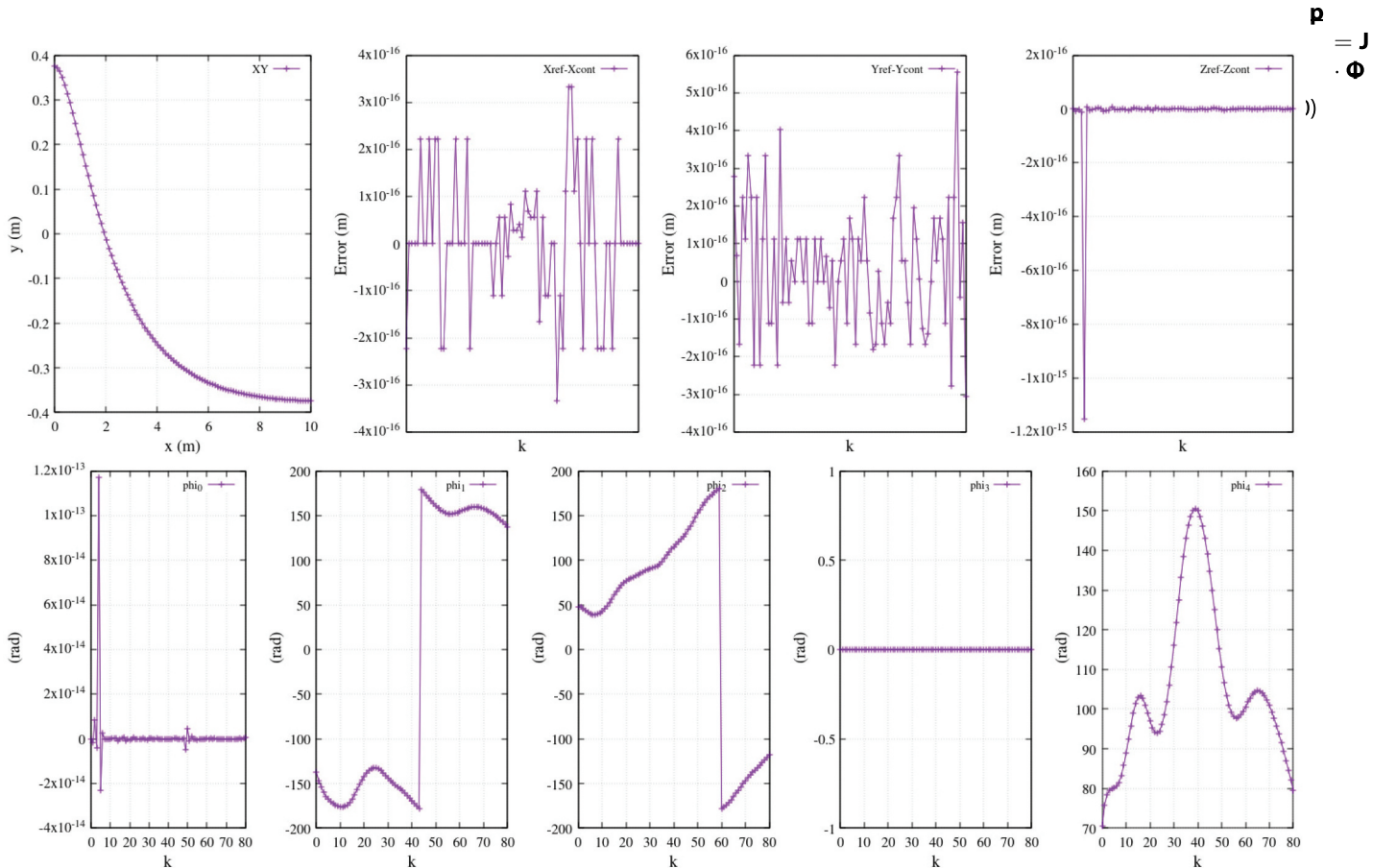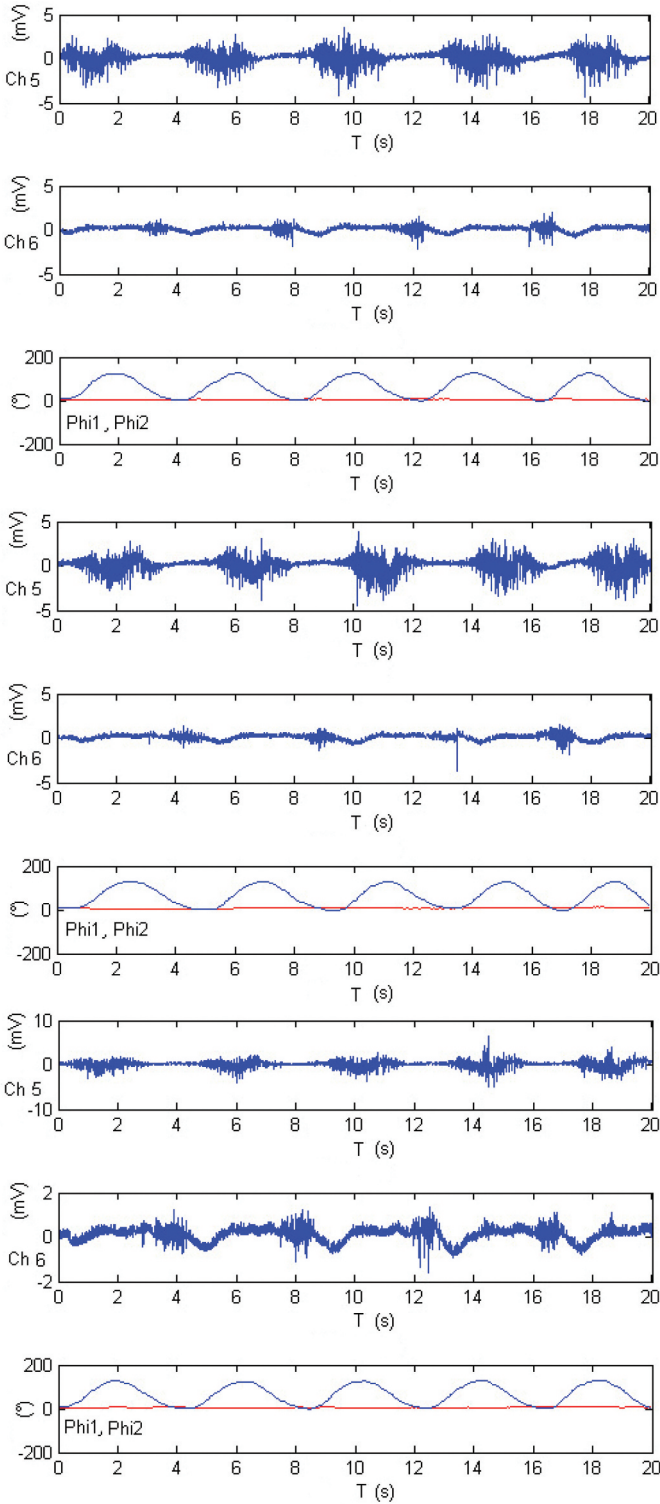

Figure 21. Metric errors of controlled planar trajectory versus a reference ($\mathbf{p}^{ref} - \mathbf{p}_t$). Tracking $y(x) = \kappa_1 \cos\left(\frac{\kappa_2 x}{x + \kappa_3}\right)$.

Figure 22. Calibrated EMG measurements, estimation joints' angle ϕ_1 and ϕ_2 in elbow-flexion performance.

and stating this expression in the form of differential equation, its derivative-order decreases

$$\frac{d\mathbf{p}}{dt} = \mathbf{J} \cdot \frac{\mathbf{\Phi}}{dt}, \tag{71}$$

completing all differentials with their respective integrals at both sides of the equality

$$\int_{\mathbf{p}_1}^{\mathbf{p}_2} d\mathbf{p} = \mathbf{J} \cdot \int_{\mathbf{\Phi}_1}^{\mathbf{\Phi}_2} d\mathbf{\Phi}, \tag{72}$$

therefore, the expression (78) is the general recursive solution,

$$\mathbf{p}_{t2} - \mathbf{p}_{t1} = \mathbf{J} \cdot (\mathbf{\Phi}_{t2} - \mathbf{\Phi}_{t1}). \tag{73}$$

Therefore, from such an equality the expressions (74) lead to forward/backward general solutions. The recursive forward:

$$\mathbf{p}_{t+1} = \mathbf{p}_t + \mathbf{J}_t \cdot (\mathbf{\Phi}_{t+1} - \mathbf{\Phi}_t) \tag{74a}$$

and the recursive backward:

$$\mathbf{\Phi}_{t+1} = \mathbf{\Phi}_t + \mathbf{J}_t^+ \cdot (\mathbf{p}_f - \mathbf{p}_t). \tag{74b}$$

Therefore, the inverse general model for the recursive control law is set by an ideal global trajectory $\mathbf{p}_t^{ref}$,

$$\mathbf{\Phi}_{t+1} = \mathbf{\Phi}_t + \mathbf{J}_t^+ \left(\mathbf{p}_t^{ref} - \hat{\mathbf{p}}_t\right). \tag{75}$$

Some terms in the model are expanded. Since the Jacobian is non-squared, a pseudoinverse matrix solution is applied,

$$\mathbf{\Phi}_{t+1} = \mathbf{\Phi}_t + (\mathbf{J}_t \mathbf{J}_t^{\mathsf{T}})^{-1} \mathbf{J}_t^{\mathsf{T}} \left[\begin{pmatrix} x_t^{ref} \\ y_t^{ref} \end{pmatrix} - \begin{pmatrix} \hat{x}(\hat{t}) \\ \hat{y}(\hat{t}) \end{pmatrix} \right] \tag{76}$$

and the forward solution has the next local reference $\mathbf{\Phi}_{t+1}$,

$$\mathbf{p}_{t+1} = \mathbf{p}_t + \mathbf{J}_t \left(\mathbf{\Phi}_{t+1} - \hat{\mathbf{\Phi}}_t\right). \tag{77}$$

Where the exoskeleton's joints direct measurements are obtained from encoder devices,

$$\mathbf{p}_{t+1} = \mathbf{p}_t + \mathbf{J}_t \left(\mathbf{\Phi}_{t+1} - \frac{2\pi}{R} \begin{pmatrix} \eta_0 \\ \eta_1 \\ \vdots \\ \eta_k \end{pmatrix} \right). \tag{78}$$

When the error condition $\| \mathbf{p}_f - \mathbf{p}_t \| > \varepsilon$ is met, the control loop achieves goal tracking. Figure 19a illustrates a complex trajectory and its tracking control performance concerning the joint angles (Figure 19b). Additionally, Figure 19c depicts the evolution of position metric errors throughout the entire reference trajectory.

In the context of numerical simulations for numerous controlled trajectories, the efficacy of the control approach was validated through a comparative analysis against a reference ideal function. The trajectory in Figure 20-above illustrates an xy path with an arbitrary reference defined as $y(x) = k_5 x^5 + k_3 x^3 - k_0$. Along the same row of the figure, the plots elucidate the error between the reference function and the controlled function. Ideally, a precise match is anticipated between the two functions. The observed errors in the x and y components, in general, are relatively small. As for the z component, its error is nearly zero since this trajectory is intentionally planar, confined solely to the xy plane. Consequently, any variation along the z axis should be virtually null. This illustration underscores the expectation that the controlled functions accurately align with a segment of a 5th-grade polynomial function.

Moreover, Figure 20-below displays the resulting errors in joints' angles induced by the trajectory in the same figure (expressed in physical units as radians).
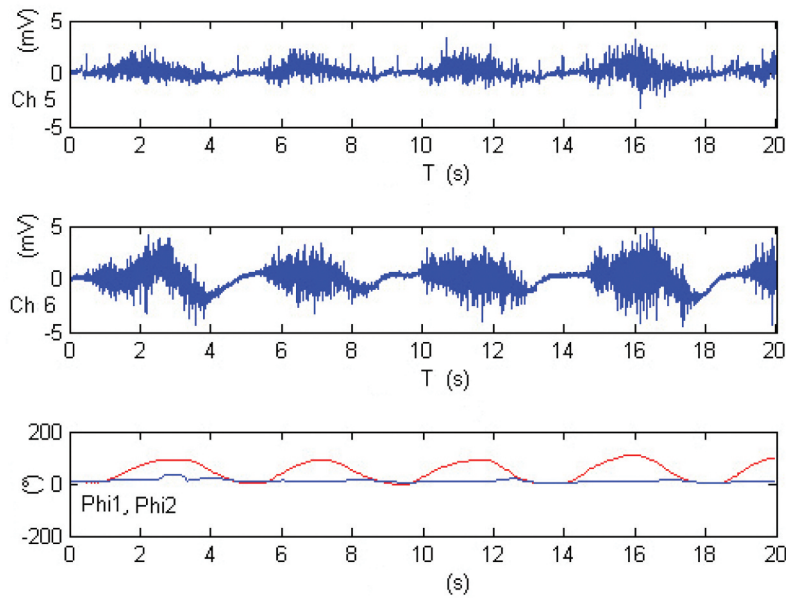
Figure 23. Calibrated EMG measurements, estimation joints' angle ϕ_1 and ϕ_2 in shoulder-flexion performance.

A comprehensive depiction akin to Figure 20, showcasing the entire joint performance, is presented in Figure 21. A distinct range of coordinates from a different reference function is established as the reference trajectory, with the framework's origin situated at the shoulder centroid. Similarly, Figure 21-above exhibits a Cartesian plot along with the errors along the three axes (reference versus controlled function). Figure 21-below illustrates the joints' angle performance resulting from the controlled tracking trajectory.

5. Results and discussion

Summarizing the core focus of this work, we direct our attention to the following three figures: Figures 22–24. These figures encapsulate the fundamental purpose and achievement of this study. They provide a visual representation of the work's primary objective, which is the estimation of joint angles from EMG measurements. For the sake of clarity and simplicity, the plots in these figures display data for two key joint angles, highlighting the remarkable success of the approach. Figure 22 presents data from three distinct experiments involving elbow flexion. Within this figure, the shoulder angle is denoted as ϕ_1 (depicted in red), and the elbow angle is represented as ϕ_2 (in blue). Two specific channels, Ch5 and Ch6, correspond to the electromyography measurements of the biceps brachii and triceps brachii, respectively. The selection of these two channels reflects the authors' recognition of their suitability for assessing electromyography activity during limb motion.
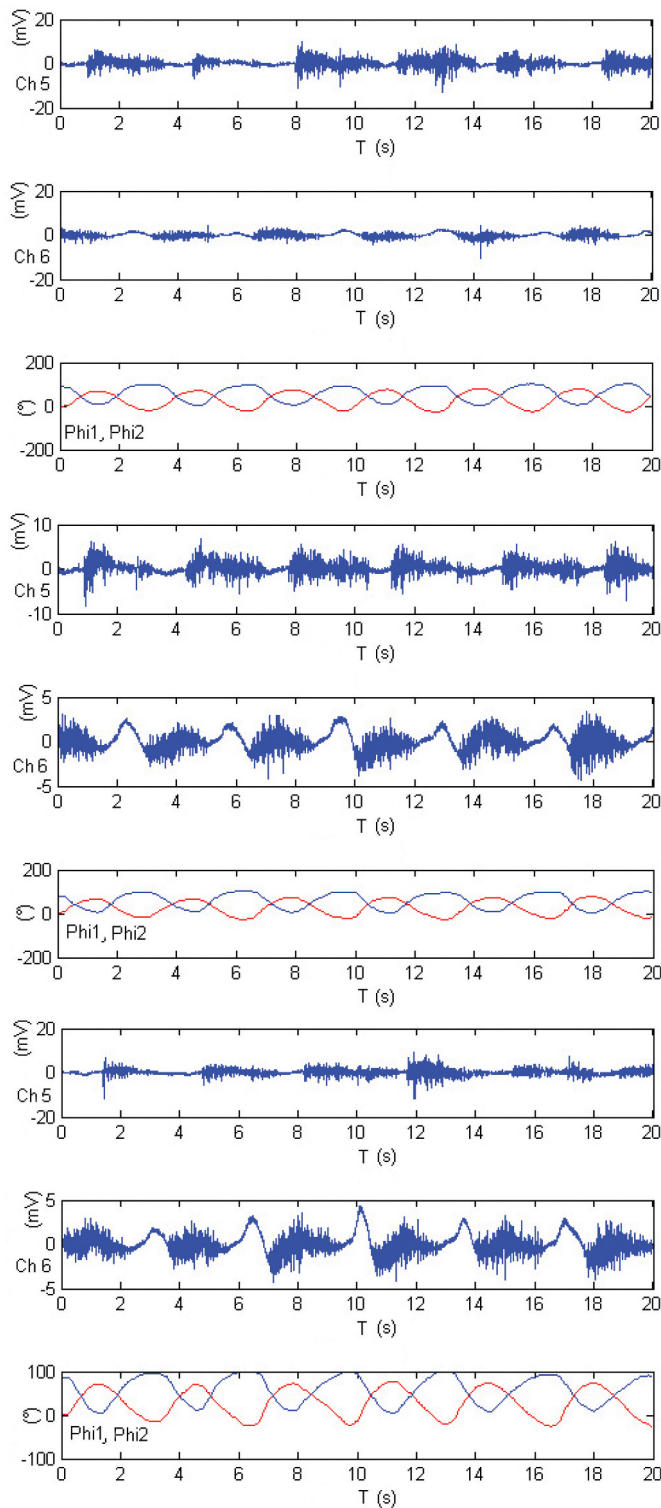
Following the calibration process, the results in Figure 22 demonstrate that the activity associated with elbow flexion (depicted in blue) reveals a strong correlation between the elevation angle and the measurements from Ch5, emphasising the crucial role of the biceps brachii in this motion. Conversely, the decrease in the elbow's angle is found to be correlated with the

measurements from Ch6, highlighting the impact of the triceps brachii. Interestingly, the motion of the shoulder joint (ϕ_1) is not detected within this specific configuration, as indicated by the red-colored plot. This observation sheds light on the distinct contributions of the two channels to the control of different joint angles.

Figure 23 offers a close look at an experiment comprising five repetitions of shoulder flexion. Within this figure, the shoulder angle continues to be represented as ϕ_1, depicted in red, while the elbow angle is identified as ϕ_2 and shown in blue. The electromyography measurements are captured by channels Ch5 and Ch6, corresponding to the activity of the pectoralis major and anterior pectoralis muscles, respectively. Following the calibration process, the results in Figure 23 reveal that during shoulder flexion activity (as depicted in the red-coloured plot), the elevation angle is strongly influenced, with substantial contributions from both Ch6 and Ch5 measurements. This highlights the role of both the anterior pectoralis and the pectoralis major muscles in controlling the shoulder's elevation angle.

However, as the exercise primarily involves shoulder motion and maintains the elbow at a fixed position, the motion of joint ϕ_2 is not detected in this particular configuration, as indicated by the blue-colored plot. This distinction further underscores the remarkable accuracy of the approach in distinguishing the contributions of different muscle groups to specific joint movements. Overall, Figure 23 demonstrates the successful application of electromyography measurements in estimating joint angles, exemplifying the adaptability and precision of this approach for diverse exercises involving multiple joints.

Figure 24 offers insight into three distinct experiments involving rowing-like flexion, wherein both shoulder and elbow joints exhibit synchronised motion activity. As in previous figures, the shoulder angle is denoted as ϕ_1, represented by the red-colored plot, while the elbow angle is identified as ϕ_2 and displayed in blue. The electromyography measurements for

Figure 24. Calibrated EMG measurements, estimation joints' angle ϕ_1 and ϕ_2 in rowing-like flexions performance.

influenced by Ch6 data. The remarkable consistency observed across these three experiments serves to validate the proposed approach in this research, showcasing the method's ability to accurately estimate joint angles during complex exercises that involve synchronised motion of multiple joints. This validation is a testament to the reliability and effectiveness of the approach, underscoring its potential for real-world applications in the field of tele-rehabilitation.

Although this study does not address more intricate rehabilitation types, the showcased exercises are representative of typical rehabilitation routines, serving as a testament to the feasibility of the proposed method. Currently, the demonstration of the model's applicability is achieved using only two EMG channels.

Given the limitation of relying on a singular visual sensor, the integration of various technological sensing devices becomes imperative. This broader array of sensing devices aims to encompass diverse perspectives surrounding the therapist's tasks, thereby enhancing the overall accuracy of measurements.

In the context of trajectory adjustment for the linear trajectory smoother model, a manual trial-and-error approach is employed to fine-tune the trajectory parameters, specifically kt and ks.

6. Conclusion

In this comprehensive research endeavour, a remarkable paradigm shift was introduced in the realm of tele-rehabilitation. The novel approach had a striking feature: therapists were no longer required to utilise additional devices during exercise teaching. Instead, they could effectively guide exercises with the utmost convenience by simply positioning themselves in front of a camera adorned with landmarks at each joint. This breakthrough allowed for asynchronous interactions, removing the constraints of rigid scheduling, as exercises could be conducted at different dates and times, making rehabilitation more accessible and flexible for patients.

The patient-exoskeleton interface was engineered to receive concise data structures, and the innovative use of coefficient sets emerged as a masterstroke. These sets proved invaluable in ensuring that data streaming remained swift and uninterrupted, unfazed by the passage of time. The application of such forward-thinking engineering principles significantly enhanced the tele-rehabilitation experience.

One of the standout features of this work was the treatment of all exercises as periodic functions. This approach enabled the seamless application of Fourier series fitting, providing an elegant and efficient means of data representation. The ability to translate complex exercises into Fourier series representations presented a new dimension of flexibility in tracking and control.

A cornerstone of this research was the ingenious method for reproducing rehabilitation exercises using Cartesian analytical polynomials. This method unlocked the door to producing high-resolution functions of time by synthesising Cartesian functions of time with EMG data, with time itself serving as the universal synchronisation variable. This synthesis represented the union of clinical precision and technological sophistication, making the rehabilitation process more accurate and efficient.

these experiments are derived from channels Ch5 and Ch6, corresponding to the activity of the middle trapezius and anterior deltoid muscles, respectively. After calibration, the results within Figure 24 reveal that elbow flexion activity (illustrated by the blue-colored plot) exhibits different oscillatory angular phases. The data suggests that the elevation of ϕ_1 appears to be significantly impacted by Ch5 measurements, while ϕ_2 is

A novel model for inferring Cartesian posture from EMG signals was a pioneering aspect of this work, showcasing remarkable reliability. The need for recalibration with each new exercise served as a testament to the adaptability and responsiveness of this approach, ensuring that the exoskeleton remained in sync with the patient's unique characteristics and movements.

The proposed exoskeleton underwent rigorous simulation testing, encompassing hundreds of tracking control rehabilitation exercises. Its adaptability was underscored by a control law that could be seamlessly adjusted to suit various exoskeleton structures, simply by readjusting the Jacobian matrix. This adaptability introduced an exciting degree of versatility and expandability in the application of this technology, not limited by specific hardware constraints.

In essence, this simulation prototype, anchored by a single reference trajectory, demonstrated remarkable potential in the calibration of numerous EMG experiments and the execution of multiple tracking control exercises. The system's adaptability, efficiency, and the profound impact it could have on the field of tele-rehabilitation were evident throughout this research. The approach outlined in this study promises to redefine and enhance the way rehabilitation is conducted, making it not just more effective but also more accessible and accommodating to a wide range of patient needs. It represents a significant step forward in the integration of technology and healthcare, and its implications are bound to be felt for years to come.

As a future work, enhancing the visual teaching process can be accomplished by substituting the RGB camera with either an RGB-D or a ranging laser device. This alternative not only mitigates noise but is also impervious to constraints and illumination variations, offering the added advantages of infrared capabilities and 3D cloud data provision.

In addition, to ensure the linear trajectory smoother model's optimal performance, automatic optimisation methods and tuning of rehabilitation trajectories, facilitated by parameters k_t and k_s, will enable a systematic convergence towards the desired reference trajectory shape.

In our forthcoming work, there is an envisioned redesign of the exoskeleton mechanism. This redesign incorporates elastic soft materials, mimicking artificial muscles activated by electrical/optical signals, preserving EMG feedback.

In addition, addressing the expansion of the EMG device array is pivotal, allowing for the comprehensive mapping of additional body muscles while utilising more compact technological devices.

We posit that exploring alternative controllers is imperative for achieving enhanced performance, tailored to different rehabilitation tasks, fostering a more nuanced understanding of optimal controller-task relationships.

Notes

1. Experimental estimations $f_h = 1.10249$ m, $f_w = 1.48499$ m.
2. The Moore-Penrose right-pseudoinverse is applied. $\boldsymbol{m}^+ = \boldsymbol{m}^{\mathrm{T}}(\boldsymbol{m}\boldsymbol{m}^{\mathrm{T}})^{-1}$

Notes on contributors

Ubaldo Castro Jiménez holds a Bachelor's degree in Biomedical Engineering from the Universidad Autónoma de Ciudad Juárez and a Master's degree in Software Engineering from the University of Texas at El Paso. With experience as a research assistant in robotics and teaching, he is currently a Software Engineer at Google.

Dr. Edgar A. Martínez-García is a Full Professor at the Universidad Autónoma de Ciudad Juárez, where he founded and leads the robotics laboratory. With a Ph.D. in robotics engineering from the University of Tsukuba and research experience at Nanyang Technological University and the Advanced Materials Research Center, Dr. Martínez focuses on robotics dynamics, control, planning, and scientific computing, bio- and neuro-robotics systems and mechanisms analysis.

ORCID

Edgar A. Martínez-García http://orcid.org/0000-0001-9163-8285

References

Aguirre-Ollinger G, Colgate JE, Peshkin MA, Goswami A. 2011. A one-degree-of-freedom assistive exoskeleton with inertia compensation: the effects on the agility of leg swing motion. Proc Inst Mech Eng Part H J Eng Med. 225(3):228–245.

Akbari A, Haghverd F, Behbahani S. 2021. Robotic home-based rehabilitation systems design: from a literature review to a conceptual framework for community-based remote therapy during COVID-19 pandemic. Front Robot AI. 8:612331. doi: 10.3389/frobt.2021.612331.

Alenabi T, Jackson M, Tétreault P, Begon M. 2013. Electromyographic activity in the shoulder musculature during resistance training exercises of the ipsilateral upper limb while wearing a shoulder orthosis. J Shoulder Elb Surg. 23(6):140–148. doi: 10.1016/j.jse.2013.08.024.

Arteaga MV, Castiblanco JC, Mondragon IF, Colorado JD, Alvarado-Rojas C. 2020. Emg-based adaptive trajectory generation for an exoskeleton model during hand rehabilitation exercises. 8th IEEE RAS/EMBS International Conference for Biomedical Robotics and Biomechatronics; 2020; New York (USA). IEEE Computer Society. p. 416–421. doi:10.1109/BioRob49111.2020.9224328.

Athwal GS. 2017. Shoulder surgery exercise Guide, american academy of orthopaedic surgeons, USA. [Online] https://orthoinfo.aaos.org/en/recovery/shoulder-surgery-exercise-guide/.

Barr JR, D'Auria D, Persia F. 2020. Telemedicine, homecare in the era of COVID-19 & beyond. International Confeerence on artificial intelligence for industries; 21-23 September 2020; CA (USA). IEEE. p. 48–51. doi:10.1109/AI4I49448.2020.00017.

Bauer G, Pan YJ. 2020. Review of control methods for upper limb telerehabilitation with robotic exoskeletons. IEEE Access. 2020(8):203382–203397. doi: 10.1109/ACCESS.2020.3036596.

Bouteraa Y, Abdallah IB. 2016. Exoskeleton robots for upper-limb rehabilitation. IEEE 13th International Multi-Conference on System, Signals and Devices; 21-24 March 2016; Leipzig, Germany. IEEE. p. 1–6.

Buongiorno D, Sotgiu E, Leonardis D, Marcheschi S, Solazzi M, Frisoli A. 2018. WRES: a novel 3 DoF wrist exoskeleton with tendon-driven

differential transmission for neuro-rehabilitation and teleoperation. IEEE Robot Autom Lett. 3(3):2152–2159. doi: 10.1109/LRA.2018.2810943.

Charafeddine J, Pradon D, Alfayad S, Chevallier S, Khalil M. 2019. Toward bio-kinematic for secure use of rehabilitation exoskeleton. Comput Met Biomech Biomed Eng. 22(sup1):s424–s426. doi: 10.1080/10255842.2020.1714968.

Cisnal A, Gordaliza P, Pérez Turiel J, Fraile JC. 2023. Interaction with a hand rehabilitation exoskeleton in EMG-Driven bilateral therapy: influence of visual biofeedback on the users' performance. Perf Sens, 23, 2048, MDPI, 2023.23(4):2048. doi: 10.3390/s23042048.

Díez JA, Catalán JM, Lledó LD, Badesa FJ, Garcia-Aracil N. 2016. Multimodal robotic system for upper-limb rehabilitation in physical environment. Adv Mech Eng. 8(9):168781401667028. doi: 10.1177/1687814016670282.

Fisahn C, Aach M, Jansen O, Moisi M, Mayadev A, Pagarigan KT, Dettori JR, Schildhauer TA. 2016. The effectiveness and safety of exoskeletons as assistive and rehabilitation devices in the treatment of neurologic gait disorders in patients with spinal cord injury. A Systematic Rev Global Spine J. 6(8):822–841. doi: 10.1055/s-0036-1593805.

Gandolla M, Ferrante S, Ferrigno G, Baldassini D, Molteni F, Guanziroli E, Cotti Cottini M, Seneci C, Pedrocchi A. 2016. Artificial neural network EMG classifier for functional hand grasp movements prediction. J Int Med Res. 45(6):1831–1847. doi: 10.1177/0300060516656689.

Goh Haoyong Yu KHLXLCH, Liu X, Goh CH, Yu H. 2006. Locomotive control of a wearable lower exoskeleton for walking enhancement. J Vibr Control. 12(12):1311–1336. doi: 10.1177/1077546306070616.

Haider I, Khan KB, Haider MA, Saeed A, Nisar K. 2020. Automated robotic system for assistance of isolated patients of coronavirus (COVID-19). IEEE 23rd Intlernational Multitopic Conference; 5-7 Nov; Bahawalpur, Pakistan. IEEE. p. 1–6. doi:10.1109/INMIC50486.2020.9318124.

He W, Li Z, Dong Y, Zhao T. 2019. Design and adaptive control for an upper limb robotic exoskeleton in presence of input saturation. IEEE Trans Neural Netw Learn Syst. 30(1):97–108. doi: 10.1109/TNNLS.2018.2828813.

He W, Sam Ge S, Li Y, Chew E, Sien Ng Y. 2015. Neural network control of a rehabilitation robot by state and output feedback. J Intell Robot Syst. 80(1):15–31. doi: 10.1007/s10846-014-0150-6.

Jiménez R, Verlinden O. 2011. Review of control algorithms for robotic ankle systems in lower-limb orthoses, prostheses and exoskeletons. J Med Eng Phys. 34(4):397–408.

Kang I, Kunapuli P, Hsu H, Young AJ. 2019. Electromyography (EMG) signal contributions in speed and slope estimation using robotic exoskeletons. IEEE 16th International Conference on Rehabilitation Robotics; 24-28 June 2019; Toronto, Canada. IEEE. p. 548–553. doi:10.1109/ICORR.2019.8779433.

Kim M, Jeong H, Kantharaju P, Yoo D, Jacobson M, Shin D, Han C, Patton JL. 2022. Visual guidance can help with the use of a robotic exoskeleton during human walking. Sci Rep. 12(1):3881. doi: 10.1038/s41598-022-07736-w.

Lanini J, Tsuji T, Wolf P, Riener R, Novak D. 2015. Teleoperation of two six-degree-of-freedom arm rehabilitation exoskeletons. IEEE International Conference on Rehabilitation Robotics; 11-14 August 2015; Singapore. IEEE. p. 514–519. doi:10.1109/ICORR.2015.7281251.

Li X, Pan Y, Chen G, Yu H. 2017. Multi-modal control scheme for rehabilitation robotic exoskeletons. Int J Robot Res. 36(5–7):759–777. doi: 10.1177/0278364917691111.

Li Z, Huang Z, He W, Su CY. 2017. Adaptive Impedance Control for an upper limb robotic exoskeleton using biological signals. IEEE Trans Ind Electron. 64(2):1664–1674. doi: 10.1109/TIE.2016.2538741.

Li Z, Wang B, Sun F, Yang C, Xie Q, Zhang W. 2014. sEMG-based joint force control for an upper-limb power-assist exoskeleton robot. IEEE J Biomed Health Inf. 18(3):1043–1050. doi: 10.1109/JBHI.2013.2286455.

Li Z, Yuan Y, Luo L, Su W, Zhao K, Xu C, Huang J, Pi M. 2019. Hybrid brain/muscle signals powered wearable walking exoskeleton enhancing motor ability in climbing stairs activity. IEEE Trans Med Robot Bionics. 1(4):218–227. doi: 10.1109/TMRB.2019.2949865.

Liu Y, Guo S, Yang Z, Hirata H, Tamiya T. 2022. A home-based tele-rehabilitation system with enhanced therapist-patient remote interaction: a feasibility study. IEEE J Biomed Health Inf. 26(8):4176–4186. doi: 10.1109/JBHI.2022.3176276.

Magid E, Zakiev A, Tsoy T, Lavrenov R, Rizvanov A. 2021. Automating pandemic mitigation. Adv Robot. 35(9):572–589. doi: 10.1080/01691864.2021.1905059.

Pons JL, editor. 2008. Wearable robots: biomechatronic exoskeletons. 1st ed. Sussex, England: Wiley and Sons.

Pu S, Pei Y, Chang J. 2020. Decoupling finger joint motion in an exoskeletal hand: a design for robot-assisted rehabilitation. IEEE Trans Industr Electron. 67(1):686–697.

Samadi B, Achiche S, Parent A, Ballaz L, Chouinard U, Raison M. 2015. Custom sizing of lower limb exoskeleton actuators using gait dynamic modelling of children with cerebral palsy. Comput Met Biomech Biomed Eng. 19(14):1519–1524. doi: 10.1080/10255842.2016.1159678.

Sarac M, Solazzi M, Frisoli A. 2019. Design requirements of generic hand exoskeletons and survey of hand exoskeletons for rehabilitation, assistive, or haptic use. IEEE Trans Haptic. 12(4):400–413. doi: 10.1109/TOH.2019.2924881.

Sun W, Peng H, Liu Q, Guo Z, Ibrah O, Wu F, Li L. 2020. Research on facial emotion recognition system based on exoskeleton rehabilitation robot. IEEE 11th Intlernational Conference on Software Engineering and Service Science; 16-18 October 2020; Beijing, China. IEEE. p. 481–484. doi:10.1109/ICSESS49938.2020.9237717.

Touil M, Bahatti L, Magri AE. 2020. Telemedicine application to reduce the spread of covid-19. IEEE 2nd Intlernational Conference on Electronics, Control, Optimization and Computer Science; Kenitra, Morocco; Dec. IEEE. p. 1–4. doi:10.1109/ICECOCS50124.2020.9314459.

Wang D, Lee K, Guo J, Yang C. 2014. Adaptive knee joint exoskeleton based on biological geometries. IEEE/ASME Trans Mechatron. 19(4):1268–1278. doi: 10.1109/TMECH.2013.2278207.

Wang H, Shi X, Liu H, Li L, Hou Z, Yu. 2011. Design, kinematics, simulation, and experiment for a lower-limb rehabilitation robot. Proc IMech J Sys Cont Eng. 225(6):860–872. doi: 10.1177/0959651811408978.

Wu Z, Chitkushev L, Zhang G. 2020. A review of telemedicine in time of COVID-19. IEEE Intlernational Conference on Bioinformatics and Biomedicine; 16-19 December 2020; Seoul, Korea. IEEE. p. 3005–3007. doi:10.1109/BIBM49941.2020.9313088.

Yang CJ, Zhang JF, Chen Y, Dong YM, Zhang Y. 2008. A review of exoskeleton-type systems and their key technologies. Proc Inst Mech Eng Part C. 222(8):1599–1612. doi: 10.1243/09544062JMES936.

Yang G, Pang Z, Deen MJ, Dong M, Zhang Y, Lovell N, Rahmani AM. 2020. Homecare robotic systems for healthcare 4.0: visions and enabling technologies. IEEE J Biomed Health Inf. 24(9):2535–2549. doi: 10.1109/JBHI.2020.2990529.

Zhang S, Fu Q, Guo S, Fu Y. 2019. A telepresence system for therapist-in-the-loop training for elbow joint rehabilitation. Appl Sci. 9(8):1710. doi: 10.3390/app9081710.

Zhu S, Jin X, Yao B, Chen Q, Pei X, Pan Z. 2016. Non-linear sliding mode control of the lower extremity exoskeleton based on human–robot cooperation. Intl J Adv Rob Syst. 13(5):172988141666278. doi: 10.1177/1729881416662788.